TECHNICKÁ UNIVERZITA V LIBERCI
Fakulta strojní

# PIV Investigation of the Bluff Body in Water

## Diplomová práce

*Studijní program:* N2301 – Mechanical Engineering
*Studijní obor:* 2302T010 – Machines and Equipment Design

*Autor práce:* **Surendaran Kathiresan**
*Vedoucí práce:* Ing. Petra Dančová, Ph.D.

Liberec 2019

TECHNICAL UNIVERSITY OF LIBEREC
Faculty of Mechanical Engineering

# PIV Investigation of the Bluff Body in Water

## Master thesis

*Study programme:* N2301 – Mechanical Engineering
*Study branch:* 2302T010 – Machines and Equipment Design

*Author:* **Surendaran Kathiresan**
*Supervisor:* Ing. Petra Dančová, Ph.D.

Liberec 2019

TECHNICAL UNIVERSITY OF LIBEREC
Faculty of Mechanical Engineering

Master Thesis Assignment Form

# PIV Investigation of the Bluff Body in Water

*Name and Surname:* **Surendaran Kathiresan**
*Identification Number:* S17000476
*Study Programme:* N2301 Mechanical Engineering
*Specialisation:* Machines and Equipment Design
*Assigning Department:* Department of Power Engineering Equipment
*Academic Year:* **2018/2019**

**Rules for Elaboration:**

This thesis deals with the experimental investigation of the flow around the bluff body in water as a working fluid. The PIV method for velocity fields investigation is used.

1. Make the state of art of the problem.
2. Design the experimental setup and the bluff body (cylinder with a slot inside).
3. Perform the 2D PIV experiments of the bluff body and with the (full) cylinder. Compare and describe these experiments according to the fluid dynamics theory.
4. Analyze your data and do the comparison with the literature.

| | |
|---|---|
| *Scope of Report:* | up to 50 pages |
| *Thesis Form:* | printed |
| *Thesis Language:* | English |

**List of Specialised Literature:**


[1] WIENEKE, Bernhard. PIV Uncertainty Quantification and Beyond. *Unpublished* [online]. 2017 [vid. 2019-04-25]. Dostupné z: doi:10.13140/rg.2.2.26244.42886

[2] NEETESON, N. J., S. BHATTACHARYA, D. E. RIVAL, D. MICHAELIS, D. SCHANZ a A. SCHRÖDER. Pressure-field extraction from Lagrangian flow measurements: first experiences with 4D-PTV data. *Experiments in Fluids* [online]. 2016, 57(6) [vid. 2019-04-25]. ISSN 0723-4864, 1432-1114. Dostupné z: doi:10.1007/s00348-016-2170-4


| | |
|---|---|
| *Thesis Supervisor:* | Ing. Petra Dančová, Ph.D.<br>Department of Power Engineering Equipment |
| *Date of Thesis Assignment:* | 1 November 2018 |
| *Date of Thesis Submission:* | 30 April 2020 |

Technická univerzita v Liberci -8- L.S.

prof. Dr. Ing. Petr Lenfeld
Dean

doc. Ing. Václav Dvořák, Ph.D.
Head of Department

Liberec 1 February 2019

# Declaration

I hereby certify I have been informed that my master thesis is fully governed by Act No. 121/2000 Coll., the Copyright Act, in particular Article 60 – School Work.

I acknowledge that the Technical University of Liberec (TUL) does not infringe my copyrights by using my master thesis for the TUL's internal purposes.

I am aware of my obligation to inform the TUL on having used or granted license to use the results of my master thesis; in such a case the TUL may require reimbursement of the costs incurred for creating the result up to their actual amount.

I have written my master thesis myself using the literature listed below and consulting it with my thesis supervisor and my tutor.

At the same time, I honestly declare that the texts of the printed version of my master thesis and of the electronic version uploaded into the IS STAG are identical.

K. Surendaran

29. 4. 2019 Surendaran Kathiresan

# ACKNOWLEDGEMENT

I would like to express my sincere gratitude towards everyone who extended their priceless support for this endeavour.

Special thanks to Ing. Petra Dančová, Ph.D., supervisor of my thesis, for her guidance and support throughout my Master thesis.

I would like to thank my Head of the department, doc. Ing. Václav Dvořák, Ph.D., and Technical University of Liberec for the opportunity presented.

Finally, I would like to thank my family and friends for their support throughout my career.

This publication was written at the Technical University of Liberec as part of the project " Experimental, theoretical and numerical research in fluid mechanics and thermo-mechanics, no. 21291“ with the support of the Specific University Research Grant, as provided by the Ministry of Education, Youth and Sports of the Czech Republic in the year 2019.

# ABSTRACT

The objective of this thesis is to analyse and compare the flow around cylindrical bluff bodies in a rectangular towing tank using the Particle Image Velocimetry Technique (PIV), in which the vector fields and relative properties are analysed. Water at room temperature is utilized as the fluid medium and glass spheres are used as the seeding particles to view the flow around the bodies. The fluid flows along a rectangular cross section with a length of 2 metres and the bluff bodies are placed 1.5 metre away from the entrance of the fluid with a honeycomb structure placed in the entrance to get a streamlined flow. The flow around bluff bodies are investigated for two Reynolds number with values 748.5 and 499, and have been analysed for properties like vortex shedding, flow separation region, etc.

***Keywords:*** Bluff bodies, Particle Image Velocimetry, Reynolds number, Honeycomb.

# TABLE OF CONTENTS

# LIST OF FIGURES

# LIST OF SYMBOLS

| | | |
|---|---|---|
| $\tau$ | Drag force | (N) |
| $Re$ | Reynolds number | (1) |
| $\rho$ | Fluid density | ($kg/m^3$) |
| $v$ | Velocity of the fluid | (m/s) |
| $\mu$ | Dynamic viscosity | (Pa-s) |
| $D$ | Pipe diameter | (m) |
| $D_h$ | Hydraulic diameter | (m) |
| $Q$ | Volumetric flow rate | ($m^3/s$) |
| A | Cross sectional area of test section | ($m^2$) |
| $St$ | Strouhal number | (1) |
| $f_w$ | Vortex shedding frequency | (Hz) |
| $C_s$ | Scattering cross section | ($m^2$) |
| $d_p$ | Particle diameter | (m) |
| $\rho_p$ | Particle density | ($kg/m^3$) |
| $\rho_f$ | Fluid density | ($kg/m^3$) |
| $\hat{U}_p$ | Instantaneous velocity of particles | (m/s) |
| $\hat{U}_f$ | Instantaneous velocity of fluid | (m/s) |
| $\hat{V}$ | Instantaneous relative velocity | (m/s) |
| $d_g$ | Diameter of mean image geometry | (m) |
| $d_e$ | Effective particle diameter | (m) |
| $d_s$ | Particle diameter in image plane | (m) |
| $d_r$ | Minimum resolution of recording media | (Pixels per unit area) |
| $R_r$ | Relative dynamic range | (1) |

# LIST OF ABBREVIATIONS

| | |
|---|---|
| CCD | Charged Coupled Device |
| DFT | Discrete Fourier Transformation |
| FT | Fourier Transformation |
| FFT | Fast Fourier Transformation |
| HPIV | Holographic Particle Image Velocimetry |
| MART | Multiplicative Algebraic Reconstruction Technique |
| Nd:YAG | Neodymium-doped Yttrium Aluminum Garnet |
| PTU | Programmable Timing Unit |
| PIV | Particle Image Velocimetry |
| PTV | Particle Tracking Velocimetry |
| sCMOS | scientific Complementary Metal-Oxide-Semiconductor |
| TomoPIV | Tomographic Particle Image Velocimetry |
| VIV | Vortex Induced Vibrations |
| μPIV | Micro Particle Image Velocimetry |

# 1. INTRODUCTION

The main purpose of this Master thesis is to have clear information about the fluid flow around a body at different velocities, so as to determine the effects of the velocity on different cross sections of the body and the flow properties. The flow of a fluid around a body is characterized with a separation of the fluid behind the body, depending on the shape, structure and other parameters. This separation of the flow of a fluid causes vortices to form in a periodic manner, which forms the Karman Vortex Street. This vortex induces vibrations of the bodies, noises and sometimes structural collapse. Limitation of such problem requires an in depth understanding of the flow field. Flow over a bluff body has been a stimulating problem for decades. This kind of flow is considered to be important because they provide potential failures to many structures. Structures like high buildings, bridges, off-shore pipelines, and risers may be considered as bluff bodies, and the study of flow around them, can improvise the betterment and life of the structure. These bodies are called bluff bodies, as they have opposing effects to the flow field. Streamlined bodies can be considered as bluff bodies at high angles of attack, which help in the study of an airplane wing at high angle of attack. Bluff bodies can be of different section, like circular, rectangular or triangular. Bluff bodies with circular cross section are of more interest, from industrial and researcher's perspective because of its wide usage in engineering applications. Applications of circular cross section include structures like, pipelines, heat exchangers, cooling tower, etc. This importance for flow over cylindrical cross section is also because of the easier analysis and simulation, as the geometry is simpler and has all potential parameters of a bluff body flow. [1]

As stated above, when a body flows through a fluid, commonly witnessed flow behaviours are flow separation and vortex shedding in the near wake downstream of the bluff body. At the point of separation, shear layer with no stability arises, which rolls up to the formation of vortices. Motions caused by the flow due to the contact between fluid and the structure, causes vortex induced vibrations (VIV), which leads to the failure of the structure in many cases. When the frequency of vortex shedding and the natural frequency of the oscillating structure are almost equal, it is coined as lock-in, which symbolizes VIV, which causes further vibration of structure. This results in failure of structure by vibration, acoustic noise, oscillating drag and lift forces acting on the surface of the body. The study of such flow is considered to be important, because of its wide spread application in day to day life such as mechanical, aerospace, ocean and wind engineering. Many techniques have been developed recently for altering and reducing the downstream wake flows. [2]

Particle Image Velocimetry have been used for the visualization of flow around bluff bodies, which gives the information about the velocity fields, pressure fields, vortices and many other necessary information. The research and publications on PIV has been growing exponentially since 1975. It is important to concentrate on the study of PIV, which is a potential visualization method for fluid flow, which can show the main causes of the problem and can be used for rectifying it. With PIV, the flow can be visualized in either two dimensional or three dimensional with the choice of selection of components.

# 2. LITERATURE REVIEW

Many researches have been made in the past dealing with the flow around bluff body and the optimization and proper usage of PIV. Some of the research articles related to this Master thesis are discussed in this section below.

Richard D Keane and Ronald J Adrian [3] mainly deals with the method of optimization of two pulses, planar PIV. The journal contains discussion about the crucial parameters required for the PIV system, and for the motion of fluid. According to the presented paper, six important parameters are significant during the performance and optimization of PIV. The identified parameters are particle image density, relative in-plane image displacement, the relative out-of-plane displacement, velocity gradient parameter, and the ratio of mean image diameter to the interrogation spot diameter. The study has been conducted about the parameters in relation with the case of autocorrelation interrogation. This dimensionless parameter has been studied with the help of Monte Carlo simulation and the criteria for optimization are presented.

J. Westerweel, D. Dabiri, M. Gharib [4] This paper deals with the optimization of displacement correlation peak in digital PIV using window offset. This method can be used for cross correlation of both single frame and double frame images. The study shows that, with the usage of window offset compared to the displacement, the noise level in the measurement can be reduced in a greater level. Simpler model has been used for the prediction of the effect and has been demonstrated in the analysis of the synthetic PIV of isotropic turbulence, actual measurement of grid generated turbulence and fully developed pipe flows. From the results of grid generated turbulence measurement, it was concluded that average measurement error for interrogation analysis with window offset was about 0.04 pixels. It was suggested to use the combination of window offset with a reduced window size, so as to keep the measurement error at a constant level. It is found to be effective to have interrogation with window offset and with reduced interrogation window will yield an improved spatial resolution result with the same signal-to-noise ratio.

Sreenadh Chevula, Angel Sanz-Andres, Sebastián Franchini [5] discussed the aerodynamic external pressure loads on a semi-circular bluff bodies under wind gusts. It describes the theoretical model, experimental setup and results with a closed section, low speed wind tunnel. A semi-empirical theoretical model has been proposed to fit the experimental process carried on. Parameters influencing the experimental results of unsteady aerodynamic loads are predicted. The results obtained from the experiment are fitted with the literature and the theoretical model to have a clear vision. It has been identified that the unsteady flow terms are in quadrature with the quasi-steady terms in this experiment.

Mehmet Ishak Yuce, and Dalshad Ahmed Kareem [6] investigated the numerical field of flow around similar circular and square cylinders for different Reynolds number, ranging from laminar to turbulent. The simulation analyses conducted was in two dimensional using k-omega turbulence model and software. It has been found that, in the flow field of square cylinder, the wakes are much more turbulent compared to the circular one. It has been concluded that the wake development and drag coefficient behind a square cylinder is found to be larger than circular cylinder.

Liang Huang, Yuhan Deng, Bo Wang [7] presented the numerical simulation of flow around bluff body using lattice Boltzmann method at different Reynolds number. In this research, flow around square cylinder is analysed using numerical method and MATLAB software. With the use of both, three dimensional graphs and curve graphs has been obtained. According to the theory, the variation in flow field is persistent and tends to be stable after the obstacle (bluff body). And the increase of instability is observed with the increase of Reynolds number.

Sibha Veerendra Singh, Nirmith Kumar M [8] analyses the flow behaviour around bluff bodies to get an improved thought on the flow around nose cone bluff bodies of missiles. For this, the influence of pressure is observed using CFD analysis program. Experimental and theoretical models has been presented and compared. Results shows that, the bluff body with low drag force formed on nose cone body, which when compared to spherical blunt and blunt body, the drag force has increased 0.42% and 0.5% respectively.

Dainel T Prosser, Marilyn J Smith [9] presented a paper to predict the range of angles of attack, in which the lift remains constant, in semi-infinite and infinite rectangular bluff bodies at angles of attack. Region of lift curve has been identified, where the lift remains constant. Since the constant lift region of two dimensional is not presented well in some computational studies, this model can be used for researchers to do with two dimensional simulations instead of complex three dimensional simulations.

Benjamin Levy, Pierre Brancher [10] investigated the A-pillar vortex on the side window of a car using dihedron model. Pressure fluctuation intensity can be obtained by the measurement of unsteady pressure at the wall. The flow around the wall has been analysed with the help of Particle Image Velocimetry (PIV). From the result obtained from PIV, it has been identified that the A-pillar vortex will not break down on its own, until the swirl strength goes below$\sqrt{2}$.

Sercan Yagmur and Sercan Dogan et al [11] investigated numerically and experimentally the flow field around bluff bodies of different geometries at two different Reynolds number. The bluff bodies used were of circular, square and triangular cross sections at Reynolds number 5000 and 10000. The experimental data was processed using Particle Image Velocimetry (PIV), whereas the theoretical data was analysed using LES turbulence model of ANSYS-Fluent software. The analysis was carried out with the bluff bodies placed horizontally perpendicular to the flow field. A conclusion has been made with the investigation that the wake length decreases with increase in Reynolds number. The drag coefficient was found to be greater at Reynolds number 5000 for triangular cylinder. This paper compared all the values for different cross section of bluff bodies and has suggested that the values are higher in square cylinder and lower in circular cylinder.

Antoni Alomar, David Angland, Xin Zhang [12] proposed a prediction model of roughness noise generated by bluff body at high Reynolds number, concentrating on the reduction of noise pollution from aircraft. It has been proposed and compared with the experimental results of similar case with flow around circular cylinder. Two methods are used, in which one is zero pressure gradient model and the other is based on the experimental results from flow around the cylindrical bluff body. This paper suggests that the roughness peak noise increases with roughness size, in case of zero pressure gradient models.

Z J Taylor, E Palombi, R Gurka, G A Kopp [13] investigated the flow around elongated bluff bodies with same chord-to-thickness ratio and with different leading and trailing edge at a single Reynolds number. It has been noted that the vortex parameters and shedding frequencies are influenced by the geometry. Each of the models shows the dominancy in leading edge, trailing edge and a balanced one. Observation of the models showed that the square edge model has the least value with the vortices, whereas the triangular being the highest.

Kin Hing Lo, Konstantinos Kontis [14] conducted an experimental study to investigate both time averaged and instantaneous flow over a scaled articulated lorry model, to observe the aerodynamics of automotive. The study has been conducted with fully turbulent flow, and analysed by two components Particle Image Velocimetry. Smoke visualization and surface oil flow visualization are used for the experiment. The results from the time averaged flow shows the counter clockwise rotating vortex formed by the low pressure wake region downstream of the lorry model. Stagnation point, separation bubble, separation point, upper and lower shear layers are identified during the experiment with time averaged flow. The instantaneous smoke visualization showed the formation of vortex shedding due to the interaction of wake vortex and upper shear layer.

F Scarano [15] reviewed the image processing methods in Particle Image Velocimetry (PIV). This journal paper focuses at improving the precision and spatial resolution of numerical interrogation schemes. It has been concluded that the window deformation method showed a lower noise level and small scale fluctuations with high measuring precision.

Bernhard Wieneke and Andrea Sciacchitano [16] presented the measurement uncertainties in Particle Image Velocimetry (PIV). Uncertainties in vorticity, Reynolds number stress and mean value are presented. Monte Carlo simulations are performed to detect the accuracy of uncertainties. It has been concluded from the experimental research that the uncertainty of the vorticity is calculated within 5% accuracy, when the spatial correlation error is taken into account. The uncertainties of the statistical quantities are dominated by finite sample size, when the flow fluctuations are larger. Underestimated uncertainty can be influenced, if the consideration of sample size is ineffective.

# 3. THEORETICAL DESCRIPTION

This section discusses the theoretical explanation from fluid dynamics which is forms the crucial part and basis for experimentation. Water is used as fluid for the experimentation.

## 3.1. FLUID

Fluid is a substance that can undergo deformation under applied shear stress or external force, which includes liquids, and gases. The study of flow of fluids can be coined as fluid dynamics, whereas fluid statics deals with the study of fluids not in motion. Unlike solids, in fluids, shear is a function of strain rate. Depending on this, fluids can be classified as Newtonian fluids and non-Newtonian fluids.

### 3.1.1. NEWTONIAN FLUIDS

A fluid is Newtonian, only if the viscous forces from the flow are linearly proportional to the rate of strain. Newtonian fluid must have constant viscosity tensor that does not depend on both stress and strain. While no real fluid fits the Newtonian model completely, commonly used liquids and gases are considered to be Newtonian, such as water and air. [17]

For an incompressible Newtonian fluid, the simple relation can be given as,

$$\tau = -\mu \frac{du}{dy} \tag{3.1}$$

where, $\tau$ (N) is the drag experienced in the fluid (shear stress)

$\mu$ is the viscous tensor, which is the shear viscosity of the fluid

$\frac{du}{dy}$ is the velocity component derivative relative to the displacement in perpendicular direction

Flowing liquid or gas element will suffer from external forces generated from surrounding fluid, including forces like viscous stress that can cause disturbances in the flow, which can be calculated mathematically using the above equation. It is dependent on the viscous tensor and the velocity components. The fluid is Newtonian, if the viscosity is constant. Examples of Newtonian fluids are air, water, glycerol, oils and a wide range of fluids. Newtonian fluids are the mathematical models of fluid in simpler form that accounts for viscosity of the fluid. Power law model is used to describe the behaviour of Newtonian and non-Newtonian fluids, which measures the shear stress with the strain rate as a function.

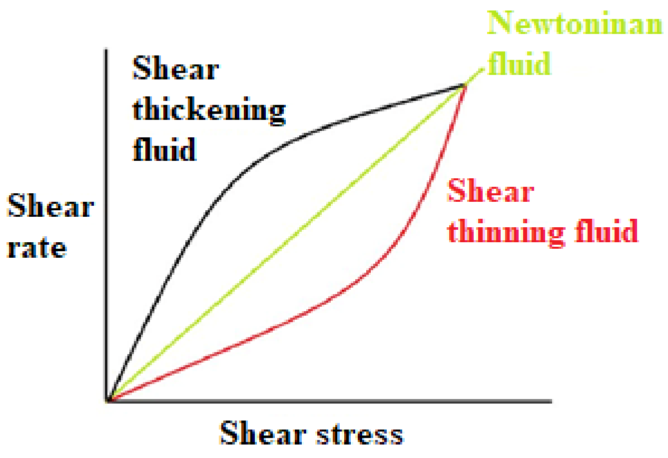


**Figure 1 Relation between shear stress and shear rate [17]**

As shown above in Figure 6, a Newtonian fluid shows linear relation between shear stress and strain rate.

### 3.1.2. NON-NEWTONIAN FLUID

A non-Newtonian fluid is a fluid that does not follow the Newton's laws of viscosity. It can be altered with external forces, either more liquid or more solid. Examples of non-Newtonian fluids are ketchup, honey, blood, corn starch, etc. This fluid does not follow the viscosity law of Newton. As in figure 6, a non-Newtonian fluid does not behave the same way, but having an exponential character. The curve above the Newtonian fluid is dilatant fluid (or Shear thickening) and the curve below the Newtonian fluid is the pseudo plastic fluid (or Shear thinning).

#### 3.1.2.1. SHEAR THICKENING FLUID

In shear thickening fluids, the viscosity increases when the rate of shear increases. For example, consider corn starch dissolved in water. The fluid acts like milk, when it is stirred slowly. The mixture acts like a fluid with high viscosity, when stirred vigorously. This is due to the thickening of shear layer, when there is high velocity from short distance. Here, the particles are randomly scattered away, and when the fluid flows, it rearranges into more compact structure.

#### 3.1.2.2. SHEAR THINNING FLUID

The fluid becomes less viscous, when shear stress is applied. The particles are more randomly scattered inside and when the shear stress is applied, they tend to rearrange themselves in an orderly fashion. For instance, considering ketchup, it can run like a liquid when squeezed from the container, but stays as a colloidal liquid, when it hits the plate.

## 3.2. REYNOLDS NUMBER

Ratio of the inertial flow of fluid to its viscous force is defined as Reynolds number. Reynolds number is used to determine the nature of fluid, whether it is laminar, transient, or a turbulent flow. Inertial force can be defined as the force due to the momentum of the mass of the fluid, whereas the viscous force can be defined as the friction, which the fluid possesses. Since both Inertial and Viscous force have the same unit, Reynolds number is dimensionless. It can also be defined as the dimensionless value, used to find the nature of the fluid. Inertial force can be given by the formula $\rho v D$, where the viscous force is given by the symbol μ. Hence the formula for Reynolds number is,

$$Re = \frac{\rho v D}{\mu} \tag{3.2}$$

where, Re ($dimensionless$) is the Reynolds number

$\rho$ ($kg/m^3$) is the fluid density in kilograms per cubic meter

$v$ ($m/s$) is the velocity in meter per second

μ ($Pa.s$) is the dynamic viscosity of the fluid in Pascal seconds

Test channels with non-circular cross section has hydraulic diameter $D_h$ in the calculation of Reynolds number. Hydraulic diameter can be determined using the area of the section $A$ and the wetted perimeter $P$. For circular channels, the hydraulic diameter and pipe diameter are same. The formula for hydraulic diameter $D_h$ for a rectangular section with height $h$ and width $w$ is,

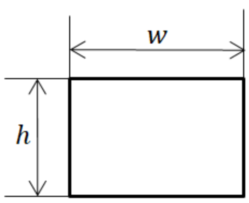


**Figure 2 Cross section of a rectangular channel**

$$D_h = \frac{4A}{P} = \frac{4 \times w \times h}{2 \times (w + h)}$$

Hence the formula for Reynolds number is,

$$Re = \frac{\rho v D_h}{\mu} = \frac{v D_h}{\nu} = \frac{Q D_h}{\nu A} \tag{3.3}$$

where Q ($m^3/s$) is the volumetric flow rate

A ($m^2$) is the area of cross section of the test channel

ν ($m^2/s$) is the kinematic viscosity which is the ratio of dynamic viscosity and fluid density.

For test channel with cylindrical cross-sections, when the Reynolds number is less than 2300, the fluid has laminar pattern of flow and when the Reynolds number crosses over 4000, it means the fluid is experiencing turbulent flow. Between 2300 and 4000, which means after laminar flow and before going to turbulent flow, the fluid experiences transient flow, which implies the transition of the fluid from laminar to turbulent, which can happen for a short period of time [18]. Whereas the test channels with non-circular, like rectangular cross-sections, the range of Reynolds number varies for different stages of flow. The Reynolds number range from 1 to 300 shows laminar flow with transient in after stage. If it is more than 300, then the vortex street is fully turbulent. For the vortex street to be visible, it is suggested to take Reynolds number from 40 to 300. [19]

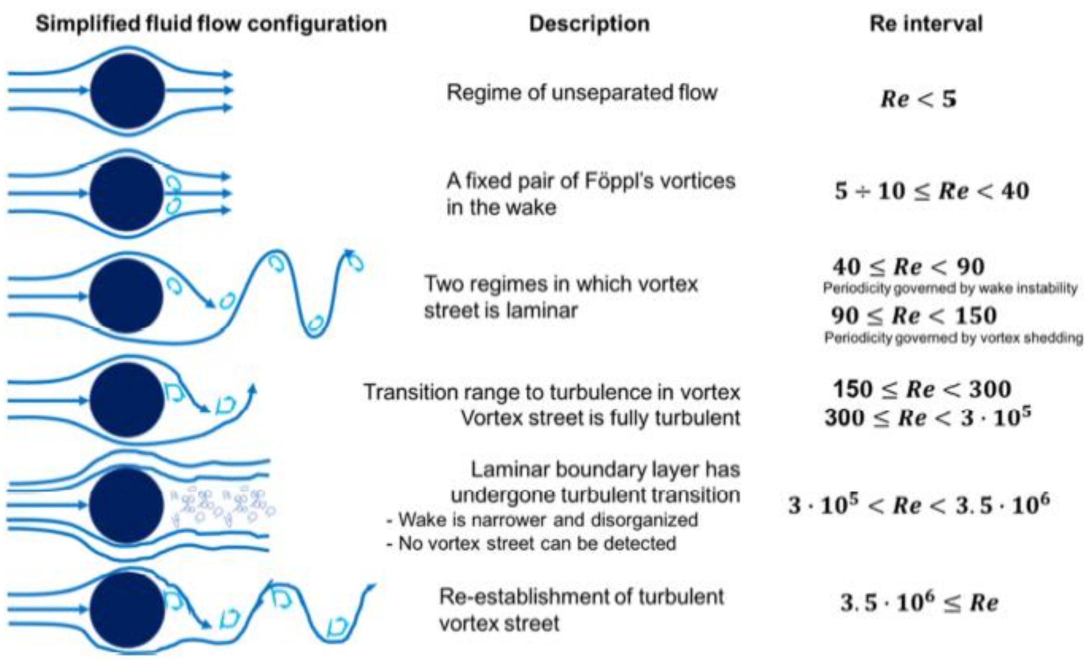


**Figure 3 Reynolds number in rectangular test channel [19]**

## 3.3. BLUFF BODY AND STREAMLINED BODY

A body moving through a flow of a fluid, experiences a force of drag which can be divided into two equal components. Drag because of frictional force and a drag because of pressure. Frictional drag comes from the contact between the fluid and the surface of the body, and the pressure drag arises from eddy motions in the fluid because of the body. Pressure drag is responsible for the formation of wakes behind any bodies. Frictional drag (or viscous drag) and pressure drag (or profile drag) can vary for different bodies. For air foils, at small angles of attack, it experiences viscous drag as the flow will have low pressure gradients and a more connected flow. At high angles of attack, the pressure gradient increases, making it more as a separated flow and the size of the wake increases. When the viscous drag dominates, the body is generally said to be streamlined body (like air foils at small angles of attack, or a fish) and when the pressure drag dominates than viscous, the body is said to be bluff body (like cylinders, spheres, or bricks). Bluff bodies are characterized by the formation of high velocity wake behind it. Near wake region will have small velocities compared to far wake regions. Far wake regions have repetitive vortices, thus forming a Kármán vortex street. [20]

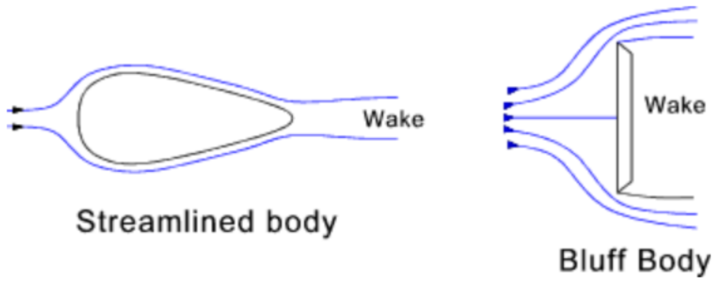


**Figure 4 Difference between streamlined body and bluff body [21]**

## 3.4. VORTEX SHEDDING

The phenomena of vortex shedding occurs when fluid flows across a bluff body, generating oscillating vortices formed on the upper and lower end of the streams. Low pressure zones are formed on the downside of the body creating fluctuating force at right angle to the fluid flow. Vortex shedding forces depend on the shape of the body used. It can also be derived using Strouhal number. Figure 5 shows the vortex shedding behind an air foil at an angle of attack of 5 degrees. If the bluff body is not mounted with caution, vibrations occurs due to the vortex shedding frequency, which when matches the natural frequency of the structure causes resonance leading to failure of the structure. Example of vortex shedding occurrence can be explained by tall chimneys constructed of thin metal walls.

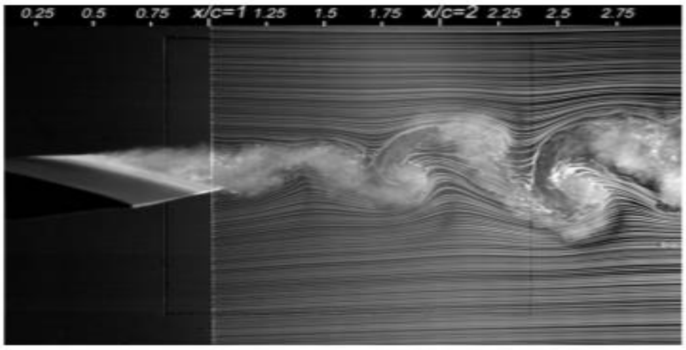


**Figure 5 Vortex shedding behind an air foil** [22]

## 3.5. KARMAN VORTEX STREET

Karman Vortex Street occurs due to the repetitive formation of swirling vortices behind a bluff body. It occurs due to the separation of the flow behind a structure. This leads to periodic pressure oscillations in both directions namely transverse and flow direction. Resonance occurs when the vortex shedding frequency is close to the natural frequency of cylinder. Karman vortex shedding frequency occurs in transverse direction, whereas in flow direction, the frequency is twice as the Karman vortex shedding frequency. Vortex shedding frequency can be defined by the term $f_w$. [23]

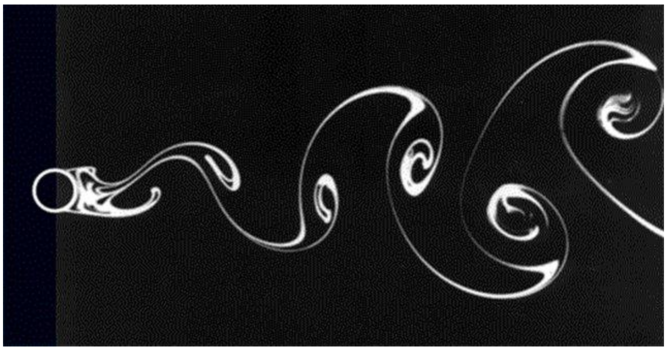

**Figure 6 Karman Vortex Street** [24]

## 3.6. STROUHAL NUMBER

Strouhal number defines the oscillating mechanisms in a flow, which is an integral part of fluid mechanics. Strouhal number depends on the frequency of vortex shedding, diameter of the body (pipe diameter or hydraulic diameter), and the velocity of the fluid flow. It also depends on the Reynolds number, which means the flow conditions. Like Reynolds number, Strouhal number is also dimensionless. The Strouhal number can be defined by,

$$St = \frac{f_w d}{V} \tag{3.4}$$

where, $St$ $(dimensionless)$ is the Strouhal number

$f_w$ $(hertz)$ is the frequency of vortex shedding

$d$ $(m)$ is the pipe diameter or hydraulic diameter normal to the flow

$V$ $(m/s)$ is the velocity of the fluid

The relation between Reynolds number and Strouhal number can be given by [25]

$$St = 0.198\left(1 - \frac{19.7}{Re}\right) \tag{3.5}$$

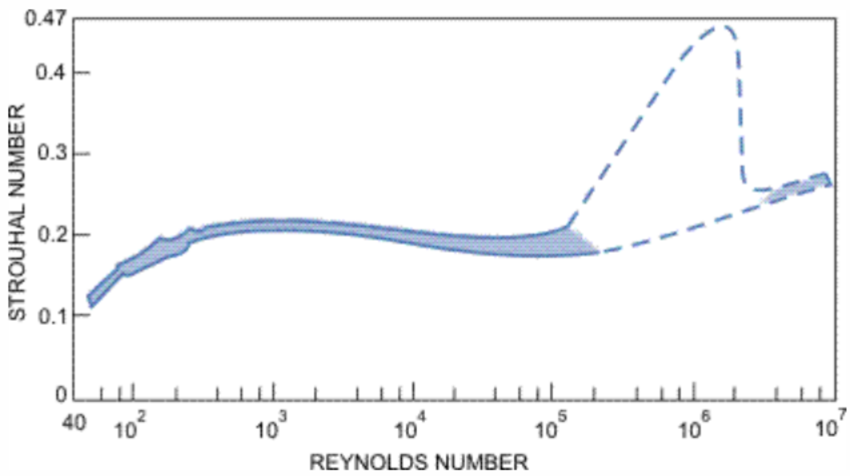


**Figure 7 Relation between Reynolds number and Strouhal Number** [25]

## 3.7. REGIMES OF FLOW AROUND CIRCULAR CYLINDER

The occurrence of vortex shedding behind a circular cylinder depends on the range of the Reynolds number used in the experiment. Depending on the Reynolds number used, the flow has been divided into different regimes based on the research done by authors until now. The flows are divided according to their boundary layer characteristics, aerodynamic forces, flow structures and vortex shedding. [26]

### 3.7.1. CREEPING FLOW

When the Reynolds number is less than 5, which is relatively low, viscous force of the fluid dominates and the boundary layer around the cylinder does not separate and leave the body. Because of the low Reynolds number, the flow around the cylinder is symmetrical both upstream and downstream. And due to this, there is no wake formation or formation of vortex shedding. Low Reynolds number implies that the flow is in laminar region.

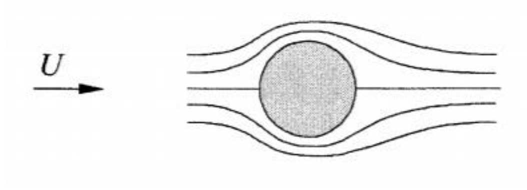


**Figure 8 Regime of creeping flow [26]**

## 3.7.2. ATTACHED EDDY FLOW

This kind of flow happens when the Reynolds number ranges from 5 to 40. In this regime, the flow of the fluid around the body starts separating from the surface of the cylinder. As it separates, the separation point starts to move upstream having the Reynolds number at 80 degrees from the stagnation point. Vortices are formed behind the cylinder, upstream and downstream. These oppositely signed vortices causes swirling movement behind the cylinder causing a recirculation zone. It can be noticed from the creep flow that the vortices increases with increase in Reynolds number.

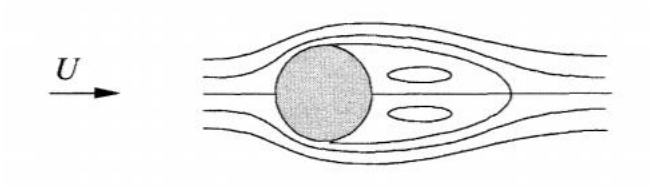


**Figure 9 Regime of attached Eddy flow [26]**

## 3.7.3. LAMINAR VORTEX SHEDDING

Laminar vortex shedding regime has Reynolds number ranging from 40 to 350. When the Reynolds number increases further than attached eddy flow, it becomes unstable and there occurs an oscillation in the shear layers. These shear layers because of the oscillation, roll up into alternating vortices. The magnitude of oscillation grows with Reynolds number until the immediate commencement of vortex shedding. These alternating vortices are shed into wakes of two rows forming oppositely signed vortices on each side, which is known as Kármán Vortex Street. The Reynolds number at which this phenomenon occurs is critical to experimental conditions such as surface roughness, and perturbations in the incoming flow. When the Reynolds number goes across 150, transition of shear layer happens, and have been subdivided by research scholars at Re=150. This is followed by discontinuity in Strouhal frequency at Re=180-190. Consecutive discontinuity occurs at Reynolds number ranging from 230 to 260.

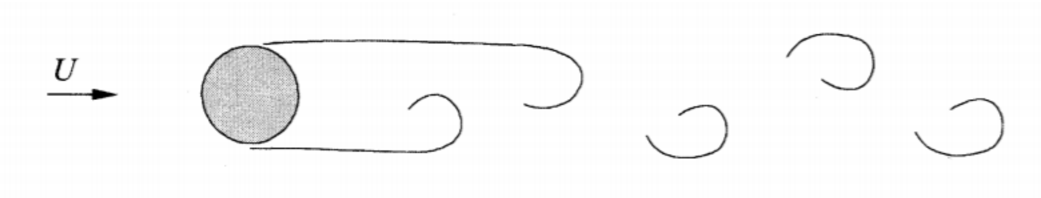


**Figure 10 Regime of Laminar Vortex Shedding [26]**

### 3.7.4. SUBCRITICAL REGIME

Coutanceau and Defaye [27] identified the flow regimes in the Reynolds number ranging from 0 to $10^7$. Ten flow regimes have been found in this range. They identified the commencing point of separation from the surface of the cylinder and a quasi-constant separation angle of approximately 80 degrees from the stagnation point. This is identified as subcritical regime with Reynolds number ranging from 350 to $2\times10^5$. In this subcritical regime, vortices occur by the transition waves in the two shear layers which is bordering the wake, which enlarges in size and rolls up. These considerably small vortices are dragged downstream by fully developed Kármán Vortex Street, having a constant Strouhal number of 0.20. With the increase in Reynolds number, these small vortices gains up energy and results in the decrease of vortex formation length. Shorter vortex formation length is a result of largest vortex shedding frequency and a small drag increase. The drag coefficient is found to be 1.2, which can be calculated with the formula,

$$Drag\ coefficient\ C_D = \frac{F_D}{\frac{1}{2}A\rho U^2} \tag{3.6}$$

Where $F_D$ (N) is the mean drag force

$A$ ($m^2$) is the frontal area of the cylinder

$\rho$ ($kg/m^3$) is the density of the fluid

$U$ (m/s) is the velocity of the flow


**Figure 11 Regime of subcritical flow [26]**

In cylinder with smooth surface, the skin friction drag accounts for 1-2% of the total drag, whereas the pressure drag accounts for remaining 98%. It has been noticed that the Reynolds number range from 1000 to $2\times10^5$ has been considered as the shear layer transition regime, where the vortex shedding behaviour remains constant. Occurrence of vortex shedding from the structure can be seen in the image below.

### 3.7.5. CRITICAL REGIME

Reynolds number with value $2\times10^5$ is considered as the critical Reynolds number for a fluid flow. This is the critical point where the flow changes from laminar to turbulent. At this point, the fluid regains the potential to reattach to the surface of the cylinder as the mixing in the boundary layer is increased. There is a sudden change in the flow behaviour and becomes sensitive to disturbances caused by roughness of the surface, turbulence of free stream and other disturbances. Then the separation bubbles that form on the surface of the cylinder becomes unstable and asymmetrical resulting in a distorted wake and a little lift force. The separation point moves downstream resulting in decrease of wake size and drag. There is a decrease in drag coefficient from 1.2 to 0.3 and a sharp increase in Strouhal number from 0.20 to 0.46, when the Reynolds number reaches $3\times10^5$.


**Figure 12 Regime of critical flow showing the separation bubbles [26]**

### 3.7.6. SUPERCRITICAL REGIME

This regime occurs when the Reynolds number ranges from $7\times10^5$ to $3.5\times10^6$. During this regime, the separation-reattachment bubble appears on both side of the cylinder and the alternating vortex shedding disappears. With the increase of Reynolds number, the separation bubble bursts and the drag coefficient increases to 0.5 to 0.7. At this point, the flow becomes turbulent and the separation bubble does not exist.


**Figure 13 Regime of supercritical flow [26]**

### 3.7.7. TRANSCRITICAL REGIME

This is the region where the flow is fully turbulent and no separation bubbles exist. This flow can be identified with Reynolds number ranging more than $3.5 \times 10^6$. There is an increase in drag coefficient from 0.50 to 0.70. Turbulent vortex shedding ends with a qausi-constant Strouhal number of 0.30. At this point, the flow is fully sensitive to external disturbances.

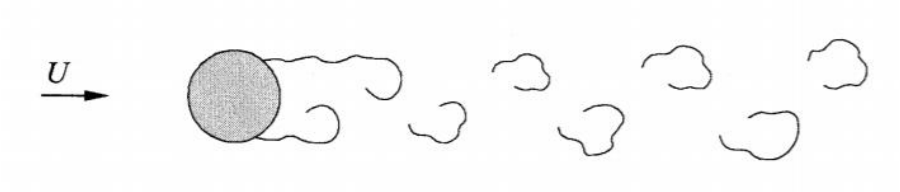


**Figure 14 Regime of Trans-critical flow [26]**

# 4. EXPERIMENTAL DESCRIPTION

Explanation of the process of experimentation using Particle Image Velocimetry, types and methods, their limitations, process of analysis using obtained results are explained in this section. In this Master thesis, Planar PIV is used for capturing the two dimensional images of velocity fields with two components.

## 4.1. PARTICLE TRACKING VELOCIMETRY

As the name suggests, Particle tracking Velocimetry (PTV) is used to measure the velocity of particles that are in a fluid. It is used for tracking the size, position, velocity, and trajectory of individual particles. This method of visualization uses Lagrangian approach for tracking individual particles. The experimentation method includes two dimensional PTV and three dimensional PTV. In two dimensional PTV (2D PTV), the flow field is measured in two dimensional planes, illuminated by a sheet of laser, having low density seeding particles to track individual particles precisely. In three dimensional PTV (3D PTV), multiple cameras are used to track the particles in a three dimensional space. Commonly used 3D PTV consists of three to four cameras focusing on the same point along the field of view. It can be used to predict the three dimensional and three component of the flow field. PTV uses charge-coupled device (CCD) cameras for capturing and processing the images, which is faster than any conventional methods.

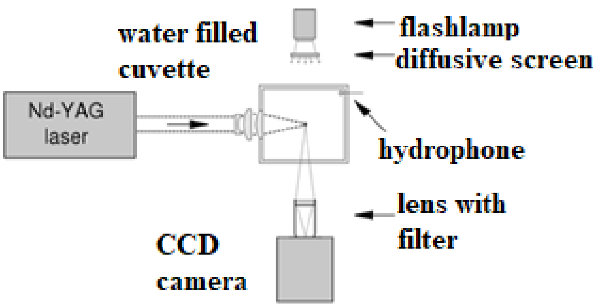


**Figure 15 Experimental setup of Particle Tracking Velocimetry [28]**

## 4.2. PARTICLE IMAGE VELOCIMETRY

An optical method used for the visualization of flow of the fluids widely used in research and development as well as in Aerospace and Automotive Industries to study the nature of the flow around an object. Particle Image Velocimetry differs from Particle tracking Velocimetry in a manner that the PIV uses Eulerian method for measuring the velocity fields, whereas PTV uses Lagrangian method for measuring the velocity components of individual tracing particles. A typical PIV setup consists of digital cameras, Laser system, a synchronizer to control laser and camera from distance, seeding particles which will be present in the fluid and the operating channel. And PIV software is used to post process the recorded images. With the help of PIV, velocity and related properties of fluids can be obtained. The fluid to be tested is seeded with tracer particles, so as to visualize the flow along the channel. Stokes number represents the degree to which the tracer particles follow the flow. The particles are illuminated using a sheet of laser for which the properties must be calculated. The displacement of the seeding particles with a relative time delay gives the velocity field of the fluid.

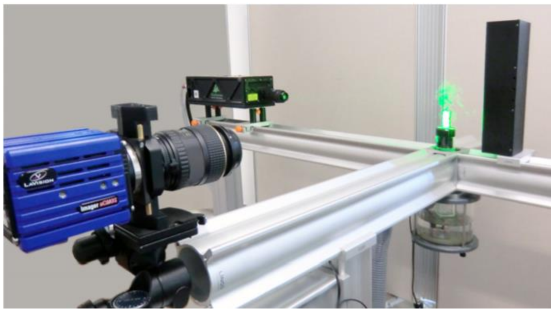

**Figure 16 Experimental Setup of Planar Particle Image Velocimetry** [Source:LaVision]

### 4.2.1. TYPES OF PARTICLE IMAGE VELOCIMETRY

The type of PIV varies depending upon the number of cameras and the kind of data measured during the experiment.

#### 4.2.1.1. PLANAR PIV

Planar PIV is used for 2 dimensional and 2 component measurement of fluid with use of single camera and a laser sheet. The camera used can be CCD or CMOS depending on the requirement. Since single camera is used, the calibration of the plane can be done easily and less time consuming compared to stereoscopic and tomographic PIV. A fiber optic cable or a liquid light guide connects the laser to the lens system. The experimental setup of planar PIV consists of a single camera, laser optics, host computer, synchronizer and the test channel with the fluid and tracer particles. The test channel is filled with the fluid and tracer particles. The laser light sheet is made to align with the field of view, so as to illuminate the particles to get a better visualization. The camera is then focussed on to the field of view, with the calibration done. The experimental setup is completed and the system is ready to capture the images. Images are captured with the range depending on the person doing the research.

These images are then post processed to get the relative velocity fields, pressure, vorticity depending on the requirements.

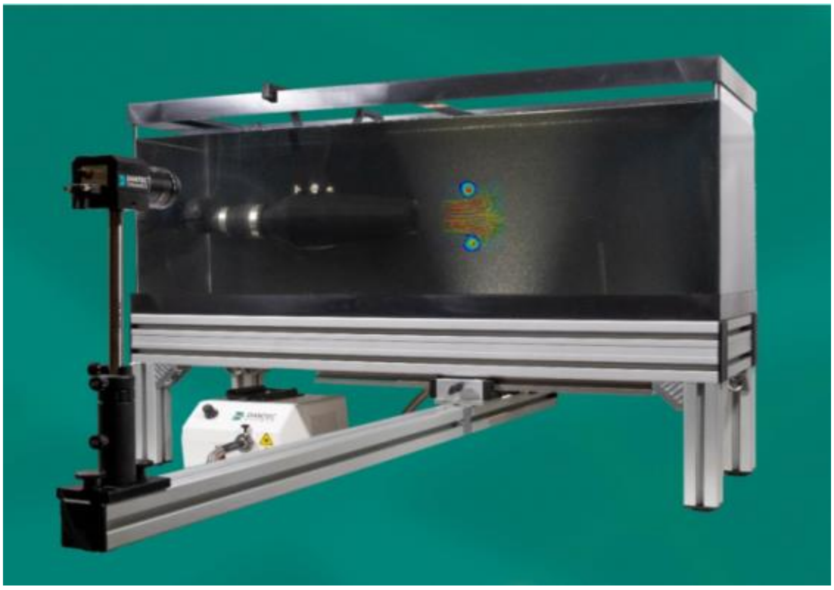

**Figure 17 Experimental setup of planar PIV [29]**

### 4.2.1.2. STEREOSCOPIC PIV

If the PIV system uses two or more cameras for measurement of third component of displacement, it can be grouped under stereoscopic PIV. Both cameras must be focused on the same point in the field of view and the calibration should be accurate to get the desired results. Advanced application of PIV is the Time resolved PIV, where the system not just captures two images but continuously recording the images, so as to give the exact flow details. With the dual camera stereoscopic PIV, x and y direction of the velocity gradients can be achieved. Stereoscopic PIV uses four cameras for the measurement, which is dual plane stereoscopic PIV. Additional plane has been added as an offset to the investigation plane in certain distance. The cameras are grouped into two, each focusing one investigation plane. This can be helpful to achieve the third direction z of the velocity gradient. Here the camera and the lens are aligned in an angle with light sheet. Because of this distortion occurs in the image field. Latest development in stereoscopic PIV includes the self-calibration method, which is helpful for rectifying the misalignment between calibration plate and laser sheet. It can be controlled from the host computer which includes software for this purpose.

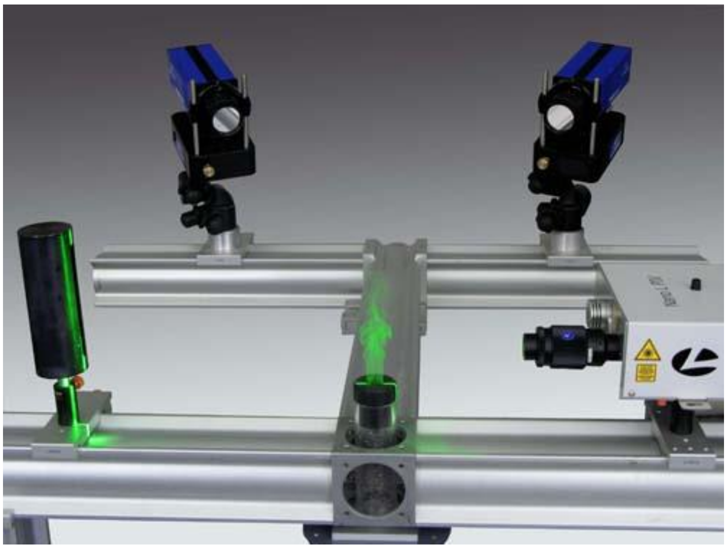

**Figure 18 2D3C Stereoscopic PIV from LaVsion [30]**

To overcome this, the angle is kept so small and the Schiempflug condition should be satisfied, which implies having a common line that is intersected with the image plane, lens plane and object plane. Since two planes is being used, a beam splitter is necessary to split the laser sheet for both the planes, so as to be viewed. The images are captured from each plane and are processed.

#### 4.2.1.3. TOMOGRAPHIC PIV

Tomographic PIV uses multiple cameras to capture the views of the illuminated volume, which is then processed to obtain the three dimensional intensity fields. Obtained 2 dimensional images get converted into 3 dimensional images, from a triangular procedure, which locates the same particle from all the cameras. In tomographic PIV, all cameras should be mapped into the same coordinate system, to get clear 3D volume visualization. The cameras should be placed approximately 30 degrees normal to the field of measurement. The volumetric calibration should be precise and effective, which should be less than 0.1 pixels to achieve good measurement volume. Multiplicative Algebraic Reconstruction Technique (MART) is a reconstruction algorithm, which is widely used in tomographic PIV to avoid the necessity to identify the individual particles. It can present full velocity and velocity gradients in three dimensional and in all the three direction. It can be helpful in the visualization of turbulent boundary layers, as the turbulent flow is three dimensional in nature.

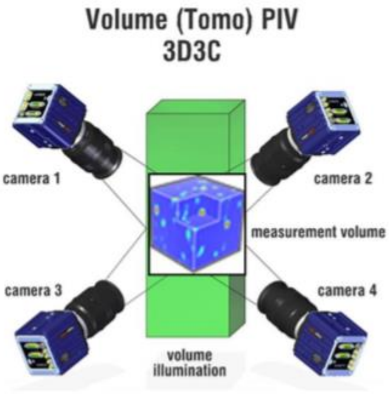


**Figure 19 Experimental setup showing Tomographic PIV** [Source:LaVision]

#### 4.2.1.4. MICRO PIV

Micro PIV or µPIV is used in microfluidics to measure the flow filed in a relatively small scale. Micro PIV uses fluorescing particles as seeding elements, which has the basic characteristics of exciting at specific wavelength and to emit at different wavelength. Micro PIV is restricted to the investigation of steady flows. Critical parameters to be considered during and before experimentation are the selection of cameras, optics, laser and seeding particles. It can present two dimensional two components system like the planar PIV and two dimensional three component system like the stereoscopic PIV.

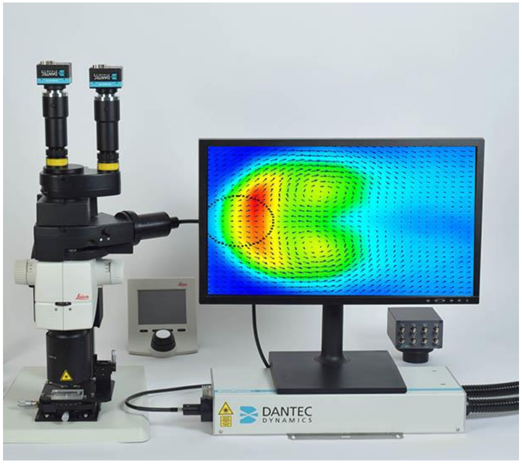


**Figure 20 Micro PIV for 2D3C measurement [31]**

### 4.2.1.5. HOLOGRAPHIC PIV

Holographic PIV (HPIV), the particle's positions present at a particular instance is recorded onto a holographic plate. The advantage of holographic PIV is that several millions of velocity vectors can be extracted from a holographic image with good quality. The experimental setup of holographic PIV includes double pulse laser system, holographic plates for image capturing, seeding particles generator, optical lenses and mirrors, CCD camera, host computer and synchronizer. The image in the holographic plate can be used to reconstruct the original intensity field by illuminating the reference beam on the holographic plate by using optics and mirrors.

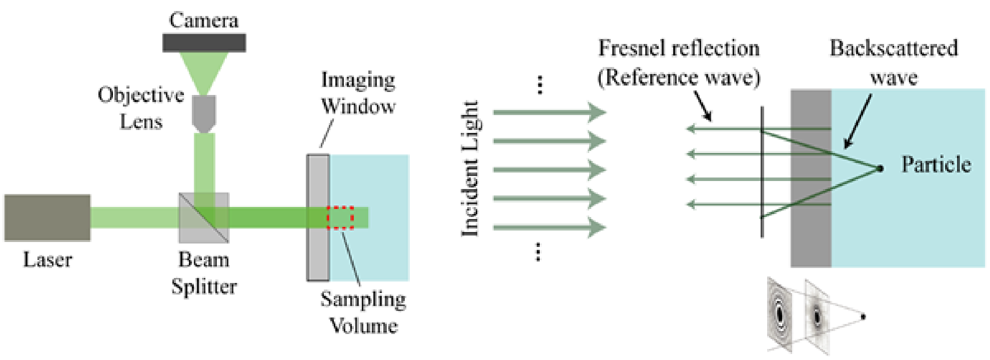


**Figure 21 Experimental setup showing the process of HPIV**

## 4.3. SEEDING PARTICLES

Seeding particles or tracer particles are the crucial part of PIV, as the seeding particles cannot be too high or too low. Seeding particles should be considered carefully such that the density of the seeding particles should be nearly equal to the density of the fluid used, so as to follow the traces of the fluid. Refractive index of the seeding particle should be different from the experimenting fluid such that the laser incident on the fluid flow reflects the particle off back to the camera. It has to be sent on an optimum level, to get the image of the flow without any disturbances. If it is high, it may cause cloud formation, and on the other hand if it is low, it will cause difficulty in capturing the images of the flow. Since, the position of the seeding particles cannot be adjusted, it is necessary to select the suitable seeding particles for the corresponding experimentations. The choice of optimal diameter of seeding particles lies between the tracer responses of the particle, which needs small diameter of seeding particle and a high signal to noise ratio, which requires larger diameters. Therefore, it is necessary to use the term scattering cross section $C_s$, which is a ratio of the total scattered power $P_s$ to the intensity of incident laser $I_0$ on the particle.

$$C_s = P_s/I_0 \quad (4.1)$$

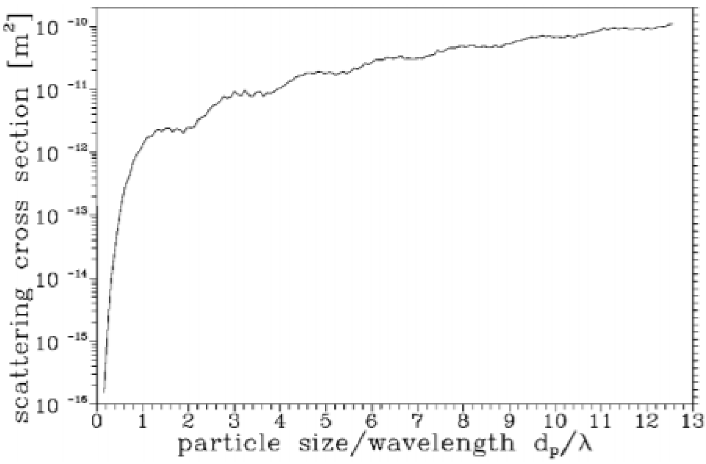


**Figure 22 Scattering cross section vs. Particle size/wavelength** [32]

Figure 22 shows the dependence of scattering cross section on the particle size at a refractive index of 1.6. The tracing capability of suspended particle depends only on the particle shape, particle diameter $d_p$, particle density $\rho_p$, fluid density $\rho_f$ and fluid dynamic viscosity μ or kinematic viscosity $\nu = \mu/\rho_f$, if the external forces like gravitational, centrifugal and electrostatic forces are considered to be negligible. Particles with irregular cross section are considered to spheres with aerodynamically equivalent diameter. The equation gives the unsteady characteristics of a sphere, as presented by Basset (1888), gives the relationship between the instantaneous velocities of the particle $\hat{U}_p$ and the fluid $\hat{U}_f$, as the instantaneous relative velocity $\hat{V} = \hat{U}_p - \hat{U}_f$ [32].

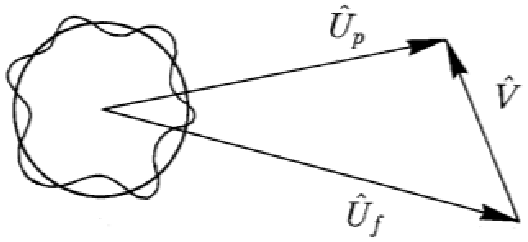


**Figure 23 Relative motion of suspended particle [32]**

The mathematical relation is given by,

$$\frac{\pi d_p^3}{6}\rho_p\frac{d\hat{U}_p}{dt} = -3\pi\mu d_p\hat{V} + \frac{\pi d_p^3}{6}\rho_f\frac{d\hat{U}_f}{dt} - \frac{1}{2}\frac{\pi d_p^3}{6}\rho_f\frac{d\hat{V}}{dt} - \frac{3}{2}d_p^2(\pi\mu\rho_f)^{1/2}\int_{t_0}^{t}\frac{d\hat{V}}{d\xi}\frac{d\xi}{(t-\xi)^{1/2}} \quad (4.2)$$

## 4.4. LASER AND OPTICS

Lasers are important part of PIV, which are used to illuminate the tracer particles to the camera. Commonly used laser system includes, Nd:YAG lasers that are able to produce high intensity lasers with short pulse duration. The laser emission is band-pass filtered for safety reasons to isolate the 532 harmonics, which is just the green light visible to the naked eye. Guiding system like fibre optics or liquid light is used to direct the laser light to the required position depending on the experiment. Optics is important to converge the laser light into a laser sheet to be incident on the field of view. Optics consists of cylindrical and spherical lenses to diverge and converge the laser into a sheet of laser.

## 4.5. CAMERAS USED IN PIV

Digital cameras with faster recording and capturing process are used like charge-coupled device (CCD) or scientific Complementary metal-oxide-semiconductor (sCMOS) which can capture two frames at high speed within few hundred nanoseconds. With the usage of this kind of cameras, various digital techniques can be implemented in PIV. It can be helpful to predict higher velocity gradients and properties using auto-correlation or cross-correlation techniques. Some has the disadvantage of low spatial and temporal resolutions.

## 4.6. SYNCHRONIZER

Synchronizer is an instrument, which acts as an external trigger, used for the control of camera and laser using the host computer. Synchronizer controls the delay time between each laser pulses $dt$ and the timing of each frame in the camera. This is helpful to establish the relation between timing of each laser pulse and the timing at which the camera captures the images.

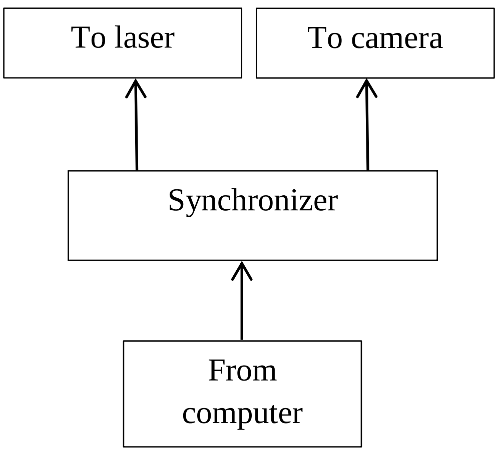


**Figure 24 Working of synchronizer**

Synchronizer can be of performance synchronizer and high performance synchronizer, which varies depending on the resolution time with less than a nanosecond. With synchronizer, it is made easily accessible to handle the time difference between laser pulses, which has been a critical problem during the measurement of PIV systems.

## 4.7. EXPOSURE METHODS

PIV exposure methods have been classified into, namely single frame method and double frame method. [33]

### 4.7.1. SINGLE FRAME METHOD

Particle's entry location in the image plane is exposed in one frame. Therefore the first image represents the initial position of the particle and the second image represents the final position of the particle. This is the method used in PIV during the past because of the conventional cameras used for recording. This can be further classified depending on the. It can be single frame single exposure, single frame double exposure or single frame multi exposure. In single frame single exposure, the exposure time is considerably long comparing to other methods. In this method, the velocity is identified by trajectory and requires low particle density. The exposure time is relatively small in double exposure method. The velocity is determined by displacement and requires some image shifting techniques. Single frame multi-exposure method has the shortest exposure time and the velocity is also determined by displacement. It can be helpful to increase the particle image number. Autocorrelation is used to process the images.

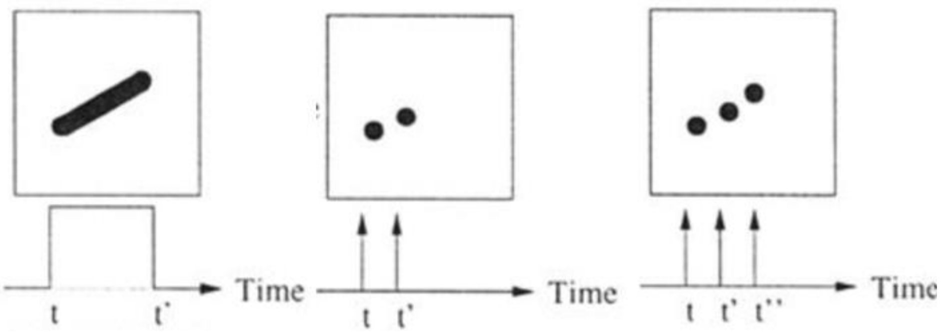


**Figure 25 Single frame a. Single exposure; b. Double exposure; c. Multi-exposure [34]**

### 4.7.2. DOUBLE/MULTI FRAME METHOD

In Double/multi frame method, the velocity is determined by the displacement between frames. It widely used in steady flows to increase the image intensity. It uses advanced CCD or sCMOS camera which can capture multiple images in relatively short time and can connect to a computer for further processing.

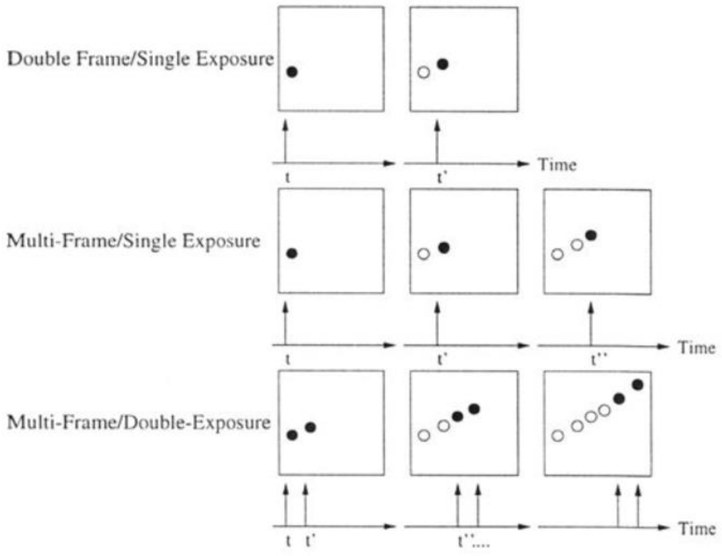


**Figure 26 Double/Multi frame methods [34]**

## 4.8. PIV IMAGE ANALYSIS

Images recorded are divided into smaller interrogation areas which are in grids. The analysis is done by determining the velocity of the flow by the displacement of particles in each interrogation window. The relation of the dimensions of interrogation area and the image plane magnification M is the ratio the ratio of object to the image,

$$\Delta x = \frac{\Delta X}{M}, \Delta y = \frac{\Delta Y}{M} \tag{4.3}$$

Where $\Delta X$ and $\Delta Y$ are the particle displacements in object plane, $\Delta x$ and $\Delta y$ are particle displacement in image plane.

The associated velocity vectors to each particle are $w_x, w_y$ in a planar PIV. The velocity vectors are determined by,

$$w_x = \frac{\Delta x}{\Delta t}, w_y = \frac{\Delta y}{\Delta t} \tag{4.4}$$

### 4.8.1. MODES OF PIV

Analysis of PIV can be performed either in auto-correlation or cross-correlation mode. In auto-correlation, the particles are illuminated multiple times in a single recording. Therefore, in analysing the auto-correlation two displacement correlation peak arise as the direction of the movement is unclear. And a self-correlation peak occurs in the centre, which may cover the displacement peaks for small displacements. Both of these effects cause an error in measuring flows, which is not contained in the dominant flow. In cross correlation mode, the particles are illuminated only once in a single recording, which insist the requirement of the successive image for measuring the flow. In cross-correlation, self-correlation does not occur. There is no directional ambiguity since the orders of images are known.

| Auto-correlation | Cross-correlation |
|---|---|
| Uses single recordings | Usage of two consecutive recordings |
| Uncertainties in directional measurement | No directional uncertainty |
| Problems with zero velocity | No such problem occurs |
| Low spatial resolution | Comparatively high spatial resolution |

Cross correlation technique is preferred these days because of the low error possibilities, with increased technology hardware and increased spatial resolution. The disadvantage of cross-correlation can be stated as the requirement of capturing two images in a relatively short time intervals.

The algorithm used for analysis of PIV is correlation which can be of two types depending on the method used. IF single exposure method is adopted, cross correlation is helpful to determine the average displacement from the evaluation area and if double exposure method is used, auto correlation can be used to determine the displacement of individual particles. PIV uses the principle of Image registration, to combine two or more images to get the desired vectors, which uses laser light sheet and seeding for visualization. More specifically, it can be called as block matching cross correlation technique, which compares two blocks from the images captured, and searches for the displacement of a particular particle from first image to second image. Likely displacement vector will have the highest peak in the correlation plane. The use of block matching technique to observe the displacement is mainly due to the minute displacement happening within the channel, which can mostly be between 5-20 pixels. So to see each speckle and their movement along, it is necessary to use block matching technique. [35].

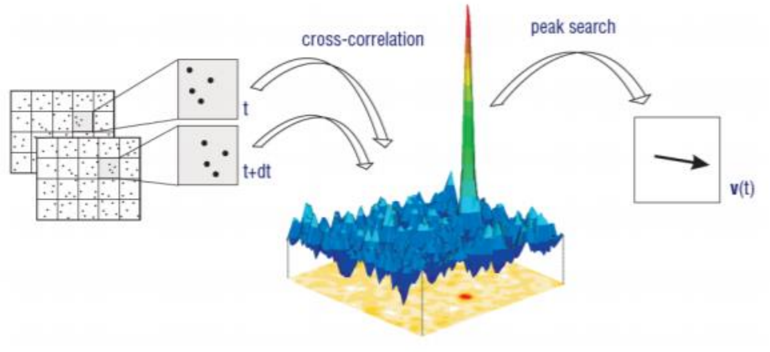


**Figure 27 Block matching cross correlation technique used in PIV** [35]

### 4.8.2. PARTICLE IMAGES

Figure shows the object plane and image plane with the optics in between. In this system of image construction, the focal length can be given by the distance of the object and images.

$$\frac{1}{f} = \frac{1}{d_o} + \frac{1}{d_i} \tag{4.5}$$

Particles are assumed to be positioned in the image plane within the depth of field of the lens of the camera

$$\delta z = 4(1 + M^{-1})^2 f^{\pi^2} \lambda \tag{4.6}$$

Where M is the magnification given by $M = {}^{d_i}/_{d_o}$

λ is the wavelength of the light

$f^{\pi}$ is the camera aperture which is the ratio between focal length and aperture diameter $D_a$

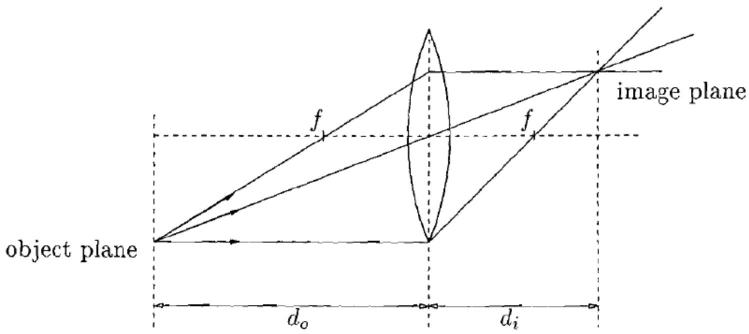


**Figure 28 Image construction [36]**

The image of finite-diameter particle is the complication of the point responses function with the particle geometry image. If the lens is diffraction limited, the point response function is determined by the Fraunhofer diffraction,

$$d_s = 2.44(1 + M)f^{\#}\lambda \tag{4.7}$$

With particles of known diameter $d_p$, the effective diameter can be defined as the diameter at which the intensity of imaged particle drops to 2.5% of its maximum .

$$d_e^2 \approx M^2 d_p^2 + d_s^2 \tag{4.8}$$

Actual size of the particle image depends on the particle size, imaging system characteristics and light source wavelength.

### 4.8.3. ENHANCING THE PRECISION AND SPATIAL RESOLUTION

Efforts to limit the correlation interrogation method corresponding to problems such as in-plane loss of pairs, velocity gradient components and correlation peak locking are made. Techniques like window offset, continuous window deformation, which come from in-plane velocity gradient. Spatial resolution of PIV method is restricted by minimum number of particles in interrogation window. Performance of PIV measurement can be optimized by solving two major problems. One deals with the hardware used during measurements and other deals with the processing of digital images. Spatial resolution can be improved by reducing the pixels of interrogation window size from a standard of 64×64 pixels, it has been reduced to 10×10 pixels under certain conditions. As the research work for PIV increases day-by-day, the result of getting misleading information with a variety of solution is a commonly faced problem. So it is important to describe the errors with a traditional tool such as counter parts. In process of PIV, reference method is numerous cross correlation function, which has features like,

- Selection of interrogation window at prescribed locations.
- Cross-correlation over two windows.
- Location of maximum correlation.
- Sub-pixel interpolation is obtained by local interpolation.

Normalized Cross correlation function

$$\phi_{fg}(m,n) = \frac{\sum_{i,j=1}^{M} f(i,j)g(i-m,j-n))}{\sqrt{cov(f)cov(g)}} \tag{4.9}$$

Where f and g describe the intensity of grey distribution over interrogation areas and the denominator is the product of covariance of images corresponding to the respective interrogation windows.

### 4.8.4. CROSS-CORRELATION

Cross-correlation is a technique used for PIV analysing. Correlation of functions f(x) and g(x) is described as the integral of the product of $f^*(x)$ with g(x) with a distance of $\Delta x$ shifted.

$$f * g = C_{fg}(\Delta x) = \int_{-\infty}^{+\infty} f * (x) g(x + \Delta x) dx \qquad (4.10)$$

Correlation is calculated for each shift $\Delta x$. Corresponding to the translation, correlation maximum appears at the shift, if a structure moves as a whole. Assuming two delta functions,

$$f(x) = \delta(x - x_f) \qquad (4.11)$$

$$g(x) = \delta(x - x_g) \qquad (4.12)$$

Correlation of the two functions is,

$$C_{fg} = \delta(x - x_{fg}) \qquad (4.13)$$

Where $x_{fg}$ is the difference between $x_g$ and $x_f$. $x_{fg} = x_g - x_f$.

Figure shows the results from correlation shows peak at $x_{fg}$ and nothing elsewhere. [36]

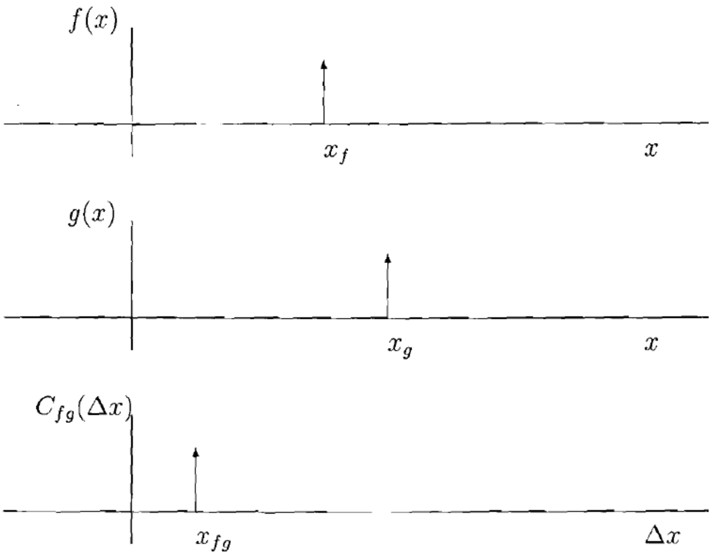


**Figure 29 Example of cross-correlation with 2 functions [36]**

Assuming that the number of points of each function equalling to N, which describes that the value of correlation is $N^2$. If the same is performed in two dimensional plane, the value increases to $N^4$. Since the number of operations becomes large very easily, it is essential to employ Fourier transformation.

### 4.8.5. CORRELATION THEOREM

To employ Fourier theory the correlation theorem has to be used. If we define a wavenumber $k$, as function of wavelength, $\lambda$, to be $k = 1/\lambda$, then the Fourier transform, $\mathcal{F}$, and the inverse Fourier transform, $\mathcal{F}^{-1}$ can be described as [36]

$$H(k) = \mathcal{F}\,[h(x)] = \int_{-\infty}^{+\infty} h(x) e^{2\pi ikx} dx, \qquad (4.14)$$

$$h(x) = \mathcal{F}^{-1}[H(k)] = \int_{-\infty}^{+\infty} H(k) e^{-2\pi ikx} dk, \qquad (4.15)$$

Correlation can be defined as,

$$Cfg\,(\Delta x) = \int_{-\infty}^{+\infty} f^*(x) g(x + \Delta x)\, dx$$

$$= \int_{-\infty}^{+\infty} \left(\int_{-\infty}^{+\infty} F^*(k) e^{2\pi ikx} dk \int_{-\infty}^{+\infty} G(k') e^{-2\pi ik'x} dk'\right) dx$$

$$= \int_{-\infty}^{+\infty} \left(\int_{-\infty}^{+\infty} F^*(k) e^{2\pi ikx} dk \int_{-\infty}^{+\infty} G(k') e^{-2\pi ik'(x + \Delta x)} dk'\right) dx$$

$$= \int_{-\infty}^{+\infty} \int_{-\infty}^{+\infty} \int_{-\infty}^{+\infty} \left(F^*(k) G(k') e^{-2\pi i(k'-k)x} e^{-2\pi ik'(x + \Delta x)} dx dk' dk\right)$$

$$= \int_{-\infty}^{+\infty} \int_{-\infty}^{+\infty} F^*(k) G(k') e^{-2\pi ik'\Delta x} \left(\int_{-\infty}^{+\infty} e^{-2\pi i(k'-k)x} dx\right) dk' dk$$

$$= \int_{-\infty}^{+\infty} \int_{-\infty}^{+\infty} F^*(k) G(k') e^{-2\pi ik'\Delta x} \delta(k' - k) dk' dk$$

$$= \int_{-\infty}^{+\infty} F^*(k) G(k) e^{-2\pi ik\Delta x} dk$$

$$= \mathcal{F}^{-1}[F^*(k) G(k)] \qquad (4.16)$$

Fast Fourier transformation are standard techniques for performing Fourier transforms.

### 4.8.6. FOURIER TRANSFORMATION

Fourier transformation (FT) can be adopted in one, two or more dimensions. Typical Fourier transform converts a function of time to its corresponding frequencies. It is used for the expression of time dependent signals using harmonic sine and cosine. Two dimensional Fourier transform can be interpreted as the distribution function of one dimensional Fourier transform.

One dimensional Fourier transform

$$F(\omega) = \int_{-\infty}^{+\infty} f(t)e^{-i\omega t}dt \tag{4.17}$$

One dimensional Inverse Fourier transform

$$f(\omega) = \frac{1}{2\pi}\int_{-\infty}^{+\infty} f(t)e^{-i\omega t}dt \tag{4.18}$$

Two dimensional Fourier transform

$$F(u,v) = \iint_{-\infty}^{+\infty} f(x,y)\, e^{-i(xu,yv)}dxdy \tag{4.19}$$

Two dimensional Inverse Fourier transform

$$f(x,y) = \frac{1}{4\pi^2}\iint_{-\infty}^{+\infty} F(u,v)\, e^{-i(xu,yv)}dudv \tag{4.20}$$

## 4.8.7. DISCRETE FOURIER TRANSFORMATION

Discrete Fourier transform (DFT) is a derivative of Fourier transformation which can be applied to a wide range of values. It is used to determine sequential samples of a function. It has discrete data, which are mostly the units of time. In discrete Fourier, the input signal is considered as a sequence of elements, like n=0,1,2,…,n=N-1,N-2,…, and so on. It uses samples with uniform intervals to produce a summation of continuous Fourier.

Discrete Fourier transformation

$$F(k) = \sum_{n=0}^{N-1} f(n)e^{\frac{-2\pi ikn}{N}} \tag{4.21}$$

Inverse discrete Fourier transformation

$$f(n) = \frac{1}{N}\sum_{n=0}^{N-1} F(k)e^{\frac{-2\pi ikn}{N}} \tag{4.22}$$

## 4.8.8. METHOD WIENEROVA - KHINCHIN THEOREM

Method Wienerova - Khinchin theorem is a method of applying a Fourier transform. This is used for the calculation of autocorrelation and cross-correlation of PIV. For identifying the results, a recording is used as first Fourier transform, and is determined by the absolute root of complex function of power spectrum. Correlation function is then achieved by applying an inverse discrete Fourier transform.

## 4.8.9. FAST FOURIER TRANSFORM

Fast Fourier transform (FFT) is an effective method for calculating discrete Fourier and its inverse. Calculating discrete Fourier transform in real time requires complex calculation and is time consuming, which can be limited by the use of FFT, which reduces the DFT matrix into product of negligible factors. It manages to reduce the complexity of DFT, and achieves the desired result. FFT uses the factor n for calculation, whereas the DFT uses $n^2$. Because of the fast activity of FFT, there might be some noise induced at the edges of evaluation area. Filter functions are used to eliminate these noises from interrogation areas.

## 4.8.10. WINDOWS FUNCTION

The error of lost pairs can be limited by the use of windows function, which eliminates the noise correlation in the borders of interrogation area due to the lost pairs and Fast Fourier transformation. Window function assigns least importance to the particles around the border, by decreasing the effect on the calculation of correlation. It can be achieved by Gauss function or Top-Hat function, which assigns zero consideration to the particles near the border and concentrating on the particles in the middle of evaluation area. Movement of large quantity particles are lost, when considering window function.

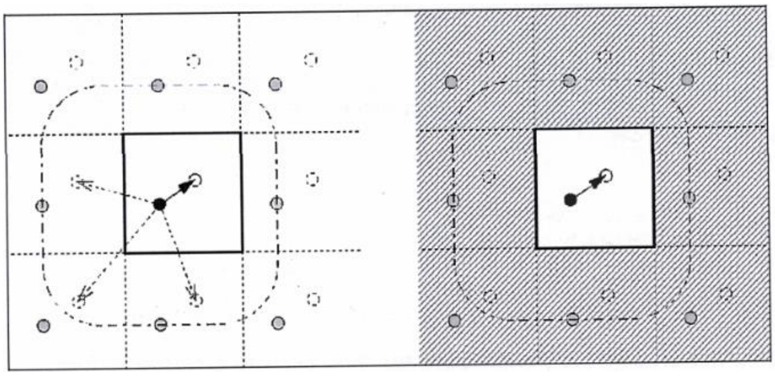

**Figure 30 Elimination of particles on the border by windows function [37]**

Windows function are portrayed with the following mathematical equation,

Top-Hat function,

$$W(m,n) = 1 \ \ when \ \frac{-kM}{2} \leq m \leq \frac{kM}{2}, \qquad \frac{-k}{2} \leq n \leq \frac{kN}{2}$$

$$W(m,n) = 0, for \ all \ other \ conditions$$

Where k determines the width of the window, (M, N) is the size of the interrogation area, and (m, n) signifies the position of pixels in the interrogation area. In the centre of the interrogation area, (m, n) = (0, 0).

Gaussian window, $$W(m,n) = exp\left[-\left(\frac{1}{k}\right)^2\left(\left(\frac{2m}{M}\right)^2 + \left(\frac{2n}{N}\right)^2\right)\right] \tag{4.23}$$

## 4.8.11. OVERLAP OF THE INTERROGATION AREA

The possibility of increasing the vector map calculation can also be by done by overlap. Overlap overcomes the limitation of windows function, where the particles from the border are neglected. In overlap, the particles in the border of first interrogation window and the particles in the border of adjacent interrogation window overlaps, and can be calculated to reduce the data loss by window function. Processing of the border particles does not increase the spatial resolution. Instead this sampling of additional vectors is helpful during the calculation of derived quantities. Disadvantage of overlap is the additional time consumed which increases with number of vectors.

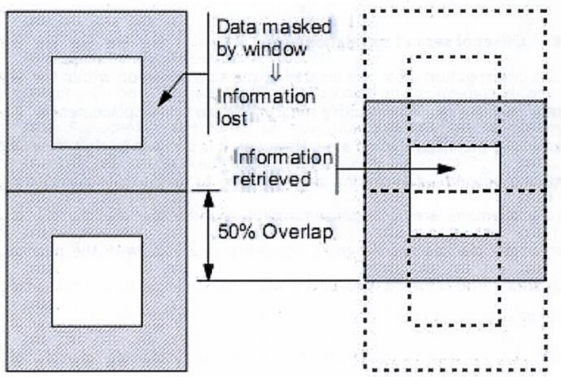


**Figure 31 Overlap of interrogation areas [37]**

## 4.8.12. SUB-PIXEL INTERPOLATION

Sub-pixel interpolation is able to identify the height, width, and placement, which is the peak location in correlation plane. Without interpolation, the maximum accuracy is restricted to the resolution of the camera used. If possible, the placement of correlation peaks in defined pixel gives the highest accuracy. It can be achieved by Gaussian curve or some other method. The peak is placed between three points in the image, which literally represents the particle. If the particle does not interfere with the points, it is suggested to adjust the camera by blurring it, and extending the image. Alternative method is to extend the correlation peak with specific filters. Width of the correlation peak should fall within the particular interval, since the interpolation cannot detect peaks with larger length, since it is also been affected by small frequency noise. This method of interpolations does not alter the final calculation of displacement.

### 4.8.13. OFFSET OF SECOND CORRELATION AREA

Interrogation areas are located in similar positions by default, within the first and second camera map. The resulting particle displacement measured is $\pm 1/4$ of the length of the side of evaluation area. It is made possible to shift the range of velocity by offsetting the second interrogation plane relative to the first. After correlating the particles of first interrogation area with the particles in second interrogation area, the resulting value found to be $\pm 1/4$ of the size of the interrogation area. Because of the offset, the particles in the first interrogation area corresponds with the particles in second interrogation area, resembling a pair, eliminating the possibility of lost par and in-plane motion. Same value of offset is applied to the whole interrogation area.

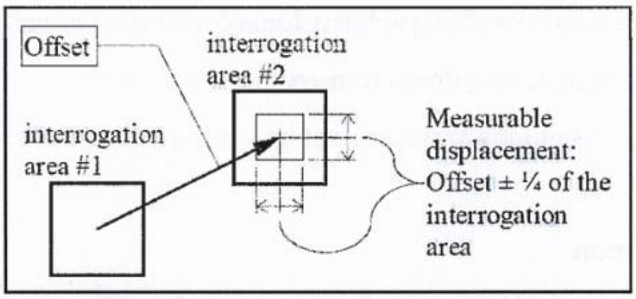


**Figure 32 Pictorial representation of offset correlation method [37]**

### 4.8.14. FILTERS

These are the filters used in frequency domain. Laser light entering into the camera can cause noise as a result of multiple reflections on the particles and optics of the camera. To reduce the noise caused by the laser light and for the protection of camera, various filters are used, depending on the process of experimentation. These filters represent the magnitude and direction of the displacement by correlating with the extending peaks.

### 4.9. UNCERTAINTY OF PIV TECHNIQUES

Methods and techniques used in PIV, some systematic errors may occur and should be considered when working with PIV systems. PIV limitations depend on size of the particle, velocity of the flow, and saturation of the seeding particles.

### 4.9.1. DYNAMIC RANGE

Performance of PIV can be valued by the measurement of parameters such as Velocity dynamic range and spatial resolution. Dynamic range describes the kinematic flow properties which covers the basic of fluid dynamics. Absolute dynamic range $R_a$ is defined as the relative difference between maximum and minimum measurable range in the interrogation area. Since the flow can take place in both directions, the motion of minimum velocity means the minimum speed in opposite direction to maximum velocity.

$$R_a = |w_{\max}| - |w_{min}| \tag{4.23}$$

Mean image geometry $d_g$ can be calculated from the relation,

$$d_g = M.d_p \tag{4.24}$$

Where $d_p$ is the diameter of the particle and $M$ is an enlargement.

Effective particle diameter $d_e$ can be calculated using a relation depending on Mean image geometry $d_g$, Actual particle diameter in image plane $d_s$, and minimum resolution of recording media $d_r$.

$$d_e = \sqrt[2]{d_g^2.d_s^2.d_r^2} \tag{4.25}$$

Minimum displacement of the particle is equal to the effective diameter of the particle. Mathematical relation for minimum displacement is,

$$|w_{min}| = \frac{d_e}{M\Delta t} \tag{4.26}$$

The maximum displacement of the particle is equal to the effective diameter of the particle that is not more than one by fourth of the interrogation length of the area. The mathematical relation for the maximum velocity is,

$$|w_{max}| = \frac{d_e}{4M\Delta t} \tag{4.27}$$

Where $\Delta t$ is the time difference between two consecutive exposures.

Relative dynamic range $R_r$ is determined by the relation of absolute values of minimum and maximum displacement.

$$R_r = \frac{|w_{max}|}{|w_{min}|} \tag{4.28}$$

From the above relations it can be concluded that the dynamic range increases with increase in area of interrogation and decreases with increase in effective diameter of the particles. The dynamic range of auto-correlation is less than that of cross correlation. [33]

Problems faced during the measurement of velocity dynamic range, [38]

- Velocity dynamic range is restricted due to the loss pairs caused by the issue between interrogation window size and in-plane displacement.
- Underestimation of velocity gradients occurs due to the finite interrogation window because of the dependence between accuracy and spatial resolution
- Peak locking occurs when the particle image sizes are smaller than two pixels or having poor spatial resolution. The phenomena of having discrete displacement values due to the dependence of displacement estimation on the peak interpolation function are called peak locking.

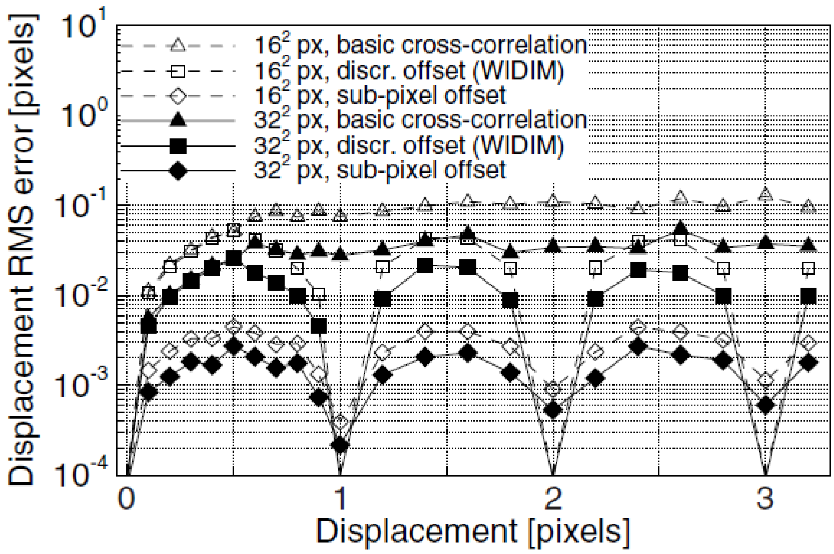


**Figure 33 Performance of correlation methods [38]**

## 4.9.2. LOST PAIRS

Lost pairs are the critical errors in PIV, which are caused when the particle leaves an interrogation area or enters an interrogation area between consecutive light pulses. Because of this lost pair, there is a chance of lonely particle in the second image, which can cause error during average velocity measurement. When dealing with turbulent flow or with high velocity, there are higher chances of the particle leaving the interrogation area, which causes the velocities with small gradients to have a greater influence during averaging calculation. This kind of gradient error is called error of velocity taking down to zero.

### 4.9.3. IMAGE SATURATION

Saturation can be poor, medium and strong. Recommended value of saturation particle is 5 per interrogation area for cross correlation and 10 particles per interrogation area for auto-correlation.

### POOR SATURATION

The efficiency of this saturation is effective if the evaluation range is not more than a single part. The determination of average displacement is simpler, but in reality, it becomes unsuitable because of the uneven spreading of the particles, where some particles are clouded in particular evaluation and missing of particles in other. Therefore, the information obtained from the images will be incomplete.

### MEDIUM SATURATION

Sufficient particles are spread along the evaluation area, so that each evaluation area gets the required amount of particles. In such case, the information on the velocity field can be easily achieved without any difficulties because of the complete information. The average displacement of all particles is determined by the use of an algorithm. This type of saturation is widely used by the researchers.

### STRONG SATURATION

Because of the high saturation, it is not possible to distinguish between individual particles, and every evaluation area becomes clouded. The image of average displacement shows a cluster of particles in the flow field. Because of this, the problem of insufficient lighting may occur.

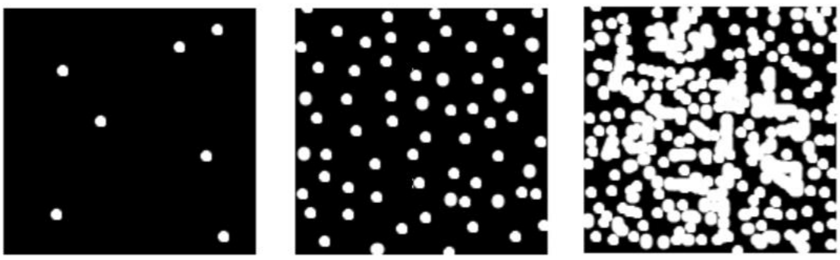

**Figure 34 a. Poor saturation; b. Medium saturation; c. Strong saturation [33]**

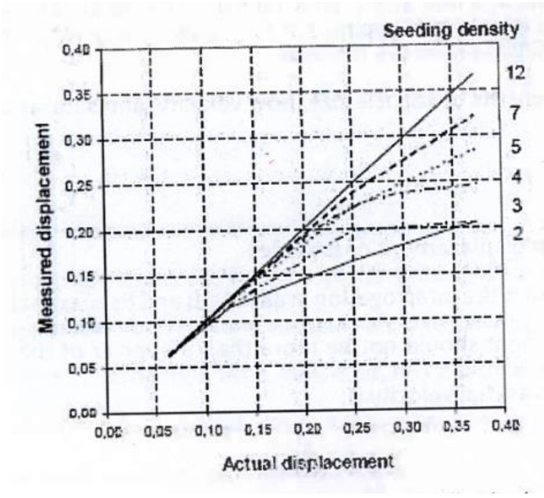


**Figure 35 Dependence of displacement on the seeding particles [37]**

### 4.9.4. MEASUREMENT ACCURACY

Main limitation for measuring accuracy includes pick-up technique, lasers and the equipment used for analysing. To get a better result from the experimentation, it is necessary to choose the reliable size of interrogation areas. Measurement accuracy, which means increasing the spatial resolution, can be attained by increasing the vectors needed in a single interrogation area. For eliminating the errors by lost pairs, it is suggested to choose interrogation areas which are considerably large. Further errors can be restricted by the use of certain techniques like overlap, window function, offset, filters, etc. These applications cannot present any new information to the calculated results, but eliminating the errors for a better visualization.

## 4.10. POST-PROCESSING OF PIV DATA

After the images are captured by the cameras, it will be stored in the host computer using software, which is to be further processed to obtain the results. Post-processing of PIV generally includes following five steps.

### 4.10.1. VALIDATION OF RAW DATA

Once the images are captured and stored, it can be able to view the raw data to check for errors. Raw data usually contains certain amount of uncertain velocity gradients that can be detected from naked eye. Because of the time consuming process, some kind of algorithm have to be developed, to be able to do it automatically. Validation of the raw data can be important because of the ability to remove certain images which can be identified as defects and will remove the error of handling improper informations.

### 4.10.2. REPLACEMENT OF IMPROPER DATA

PIV post-processing techniques require thorough information data fields to process the images to vectors. Such techniques cannot identify the vectors in the area of data drop-out, and leaves empty spaces in the result. Improvements can be made to create an algorithm for limiting this error.

### 4.10.3. DATA REDUCTION

Processed data are either reduced or grouped into pairs for the analysis, since the algorithm cannot handle all the vectors altogether. Some of them include averaging, conditional sampling, and vector field operators.

### 4.10.4. ANALYSIS

Critical part of PIV post-processing to be concentrated is analysis, as this can depend on the usage of the user to obtain the results. PIV is the first technique to deliver data about instantaneous velocity fields. And ever since, it has been an area of research in the field of fluid dynamics. Some of the analysis techniques include proper orthogonal decomposition and neural networking.

### 4.10.5. PRESENTATION OF THE INFORMATION

Wide ranges of software have been used for the purpose of presenting the PIV data. It can be presented in a varied form such as contour plotting, colour mapping, vector and scalar fields, graphical representation of numerical values. It can be helpful for the PIV user to achieve and compare the results. It is even helpful in three dimensional PIV data, which is difficult to analyse by any other method.

### 4.10.6. APPLICATIONS OF PIV

The application of PIV ranges from micrometres to meters depending on the phenomena, which implies one, can observe the flow inside blood vessels as well as the flow in rivers, ocean currents and cloud fields. Wide spread usage of PIV is for research purposes, which covers 70%, and by automotive, aerospace, chemical and medical industries, which covers 30% of the total [35]. Researches has been carried out in variety of areas which includes the usage of wind tunnel, towing tanks for water flow visualization, nozzles, flame visualization, and in biomedical researches, etc.

# 5. EXPERIMENTAL SETUP

The Experimental setup in this Master thesis, for visualization of flow of the fluid using Particle Image Velocimetry is done in several stages,

- Channel arrangement
- Design and usage of bluff bodies
- Choosing the particle tracers
- Illumination system
- Camera for capturing the images
- Host computer for post processing

## 5.1. CHANNEL ARRANGEMENT

For this master thesis, the test section used is a towing tank of rectangular cross section, which is parallelepiped by joining four glass panels with special adhesives and fasteners. Water at room temperature has been used as the working fluid for the experiment. The temperature of water during the experiment is found to be around 22 degree Celsius. The tank has a length of 200 cm, breadth of 10 cm and a height of 10 cm and Bluff body fitting is placed 150 cm away from the entry and 50 cm away from exit as shown in figure below.

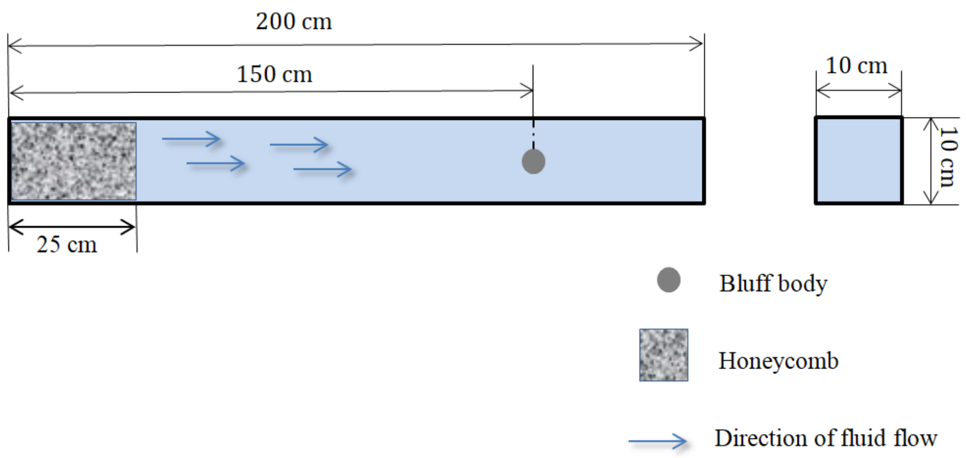


**Figure 36 Image showing the cross sectional dimensions of the tank**

Channel is fitted with pipes on both sides for entry and exit for the fluid to flow along the channel. The pump is fitted with flow meter to control the flow of water during the experiment. Since laminar flow is used for the experiment, there is a side loop of pipes, so as to reduce the flow according to the dimensions of the tank. In the entry of the tank, a storage tank of 20 litres is attached to the channel, to manage the flow, and according to the volume of the tank, which is 20000 cubic centimetre. The attachment of pump is done in such a way that the flow should be having a laminar flow as well as a streamlined flow. Tank exit has two pipes connected to it, which is then joined together to a single pipe, using a tee fitting, which then connects to pump entry. The water from the exit of the tank flows through the pump as well as a side loop which connects to the pump exit. Thus the exit water from pump is from the pump itself and the side loop. A valve has been fitted to control the flow of the water in the side loop. This then goes to the flow meter, where it can be set to different flow rates as required. From the flow meter, the water reaches the storage unit and the cycle repeats again, which has been shown in figure below. The tank has been placed in a certain height from the ground by means of aluminium pipes. The tank has been filled with water prior to the experiment to identify the leakages in the tank. It has been rectified by using special adhesives to control the leakage. The entry of the tank is fitted with thermocouple to measure the temperature of the water flowing and the water present in the tank.

**Figure 37 Setup of the channel prior to the experiment**

Honeycomb structure can be natural or man-made depending on the application where it is used. It can be available or made available in variety of geometries. As the name suggests, this honeycomb structure is an inspiration of structures of naturally occurred honeycombs. Applications of honeycomb structures include industries like automotive, aviation, sound technologies, and etc. Honeycomb structure of square cross section, which is a flow straightener, has been used at the fluid entry to get a streamlined flow along the tank. It is placed at a distance of 25 centimetres from the entry of the tank. It is used to reduce the swirling fluid motions caused at the entry. The Honeycomb consists of square hollow tubes until the end of the structure. It helps in the streamlined flow of water with seeding particles, so that the visualization is better with higher resolution.

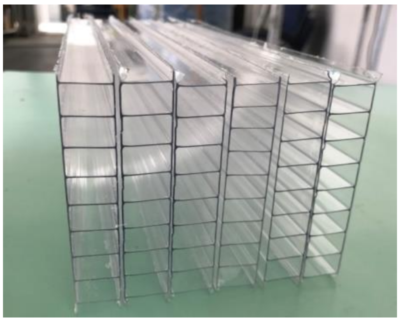

**Figure 38 Honeycomb structure used at the entrance of the tank**

## 5.2. DESIGN AND USAGE OF BLUFF BODIES

Two bluff bodies have been used in this master thesis for the experimentation of flow around bluff bodies. One of the cylinders is without slit in it and has a dimension of 10 cm in length (same like the width of the tank) and 4 mm in diameter. Since the cylinder have to be fitted inside the tank, the cylinder is manufactured with a length of 16 cm, which is when fitted into the tank, gives the constrain to 10 cm, with 3cm outside of the tank on both sides. One more cylinder is used with same cross section of the previous cylinder but with a longitudinal hole in it, with a hole of 8 cm and a width of 2 mm. The hole is placed in the centre, leaving 1 cm on each side of the cylinder. These cylinders are manufactures by 3D printing technique, because of the small dimensions used in it. Both the cylinders are used in the experiment for same flow rates and the results are obtained.

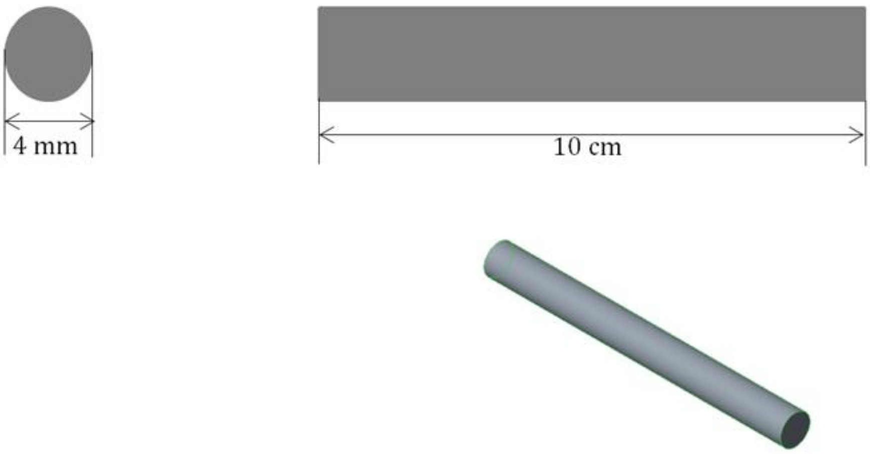


**Figure 39 Image shows the dimension of the first cylinder used in the experiment**

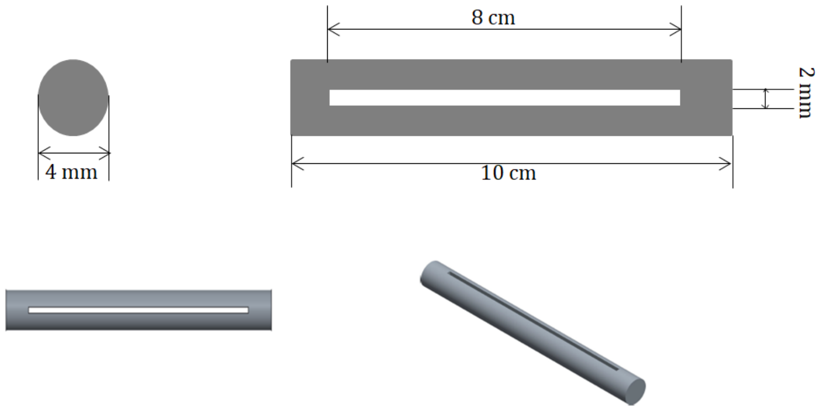


**Figure 40 Dimensions of cylindrical bluff body used in the experiment**

## 5.3. PARTICLE TRACERS

General particle tracers in water includes polymer particles, silver-covered hollow glass beams, fluorescent particles for micro flow and quantum dots, each varying in diameter and density. For this experiment with water as a fluid we are using glass hollow spheres with 9-13 $\mu m$ from LaVision GmbH. Glass spheres are borosilicate glass particles with spherical shape used preferably for liquid flow applications. Tracer particles should be used in optimum levels; such that it should not cloud the flow as well as it should be able to reflect the flow. These particles of several microns results in stronger scattering of lights

## 5.4. ILLUMINATION SYSTEM

Illumination system in PIV is composed of light source (laser) and optics. Lasers like Argon-ion laser and Nd:Yag laser are mostly used for the illumination purpose in PIV to emit monochromatic light with high energy density which can be made into a light sheet for illuminating the tracer particles inside the test channel. This sheet of light can be achieved by a set of spherical lens and a cylindrical lens which is made to incident on the area to be interrogated. The cylindrical lens expands the laser light into a plane, whereas the spherical lens converts the plane into a thin sheet. This laser sheet is incident on the area with a centimetre before the cylinder and 10-12 centimetres after the cylinder for visualization process. During the adjustment of light sheet, the lens of the camera should be covered with their caps in order to avoid the damage of the camera. Light sheet is adjusted manually to be in a straight line with the field of view, during calibration and during experimentation. It is done by using a detector or viewing card to bring it to the lowest possible thickness. Laser used in this experiment is double-pulsed Nd:Yag laser.

**Laser light specifications**

$$Quantel\ Evergreen\ 200-15\ PIV\ laser$$

$$Dual\ head\ Nd{:}YAG\ laser$$

$$200\ mJ-15\ Hz/cavity$$

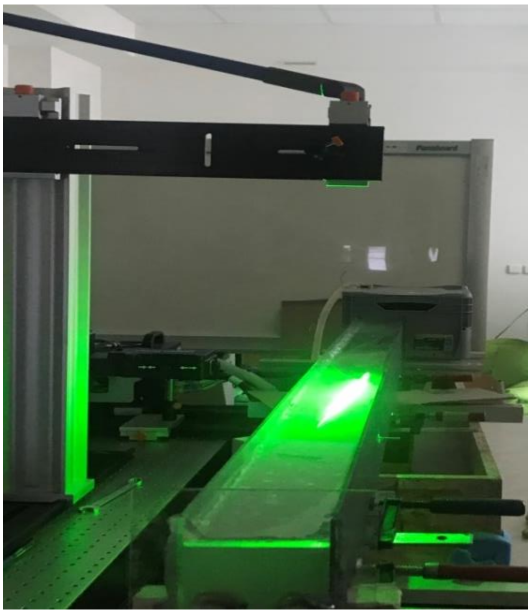

**Figure 41 Planar PIV setup with laser sheet incident on FOV**

## 5.5. CAMERA FOR CAPTURING IMAGES

sCMOS (scientific Complementary metal-oxide-semiconductor) LaVision camera is used in this process of planar PIV.

| | |
|---|---|
| Pixel resolution | $2560 \times 2160\ pixels$ ($16.6\ mm \times 14.0\ mm$ sensor size) |
| Minimum Delay time $dt$ | $120\ nanoseconds$ |
| Sensor pixel size | $6.5\mu m \times 6.5\mu m$ |
| Maximum frame rate<br>Single frame/double frame | $50\ Hz/25Hz$ |
| Grayscale resolution | $16\ bit$ dynamic range |

**Table 1 Specifications of the sCMOS camera used in the experiment**

sCMOS cameras are used for its high noise immunity and relatively low static power consumption. As this is a planar PIV, one camera is used to visualize the flow of liquid around the bluff body to measure the 2 dimensional 2 components of velocity vector. The camera can be used to capture two frames at high speed within few hundred nanoseconds as mentioned in the Table 1 above. Because of the capturing of two frames, the system uses cross-correlation analysis for processing of the images. Specific lenses have been used to capture the images like $f = -20mm$ cylindrical lens, $f/2.8$ lens with $532/10\ nm$ band pass filter. The camera and the lasers have been mounted using $X95$ rails and $X95$mounting parts, and a sliding three axis gear head. The focussing of the camera to the field of view is done by viewing the image at the computer and adjusting the aperture and the focus on the camera. A calibration sheet is used to calibrate the PIV prior to the measurements. The light sheet is aligned with the calibration sheet which is kept in the same position as the field of view. The calibration sheet consists of white dots in a black background in a perfectly machined surface for a better visualization purpose.

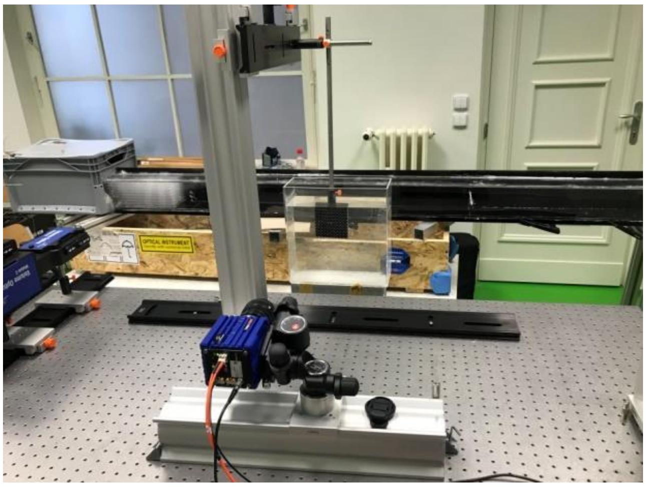

**Figure 42 sCMOS camera focussing along the field of view**

## 5.6. HOST COMPUTER

The computer system from LaVision uses dual quad-core 64 bit processing unit. It contains the LaVision's internal Programmable Timing Unit (PTU), a synchronizer from LaVision, which is used to trigger the laser and camera from the computer, which is operating the hardware using the software. It uses DaVis FlowMaster 10.0.4 software for capturing, storing, and processing the images acquired from the experiment.

## 5.7. EXPERIMENT METHODOLOGY

The experiment has been conducted after the channel is checked for leakages, laser aligned to the flow field, and the calibration have been done. Visualization of flow around bluff body has been recorded for two flow rates, which means two Reynolds number for each cylinder. The flow has been recorded at flow rate of 3 litres per minute and 4.5 litres per minute with Reynolds number of 499 and 748 respectively. 100 images are captured for each cylinder for flow rates of 3 and 4.5. The images are combined using cross correlation and are post processed.

Flow rate used: $4.5\ litres\ per\ minute$

Volumetric flow rate: $7.5 \times 10^{-5}\ cubic\ metre\ per\ second$

Cross sectional area of the test section: $0.01\ square\ metre$

Velocity of the flow: $\frac{Volumetric\ flow\ rate}{cross\ sectional\ area} = \frac{7.5\times10^{-5}}{0.01} = 0.0075\ metre\ per\ second$

Since tank used is of rectangular cross section, Hydraulic diameter should be used, during the calculation of Reynolds number.

Hydraulic diameter $D_h = \frac{4A}{P} = \frac{4 \times w \times h}{2 \times (w + h)} = \frac{4 \times 0.1 \times 0.1}{2 \times (0.1 + 0.1)} = 0.1\ metre$

$$Reynolds\ number\ Re = \frac{\rho v D_h}{\mu}$$

Where $\rho$ is the water density $1000\ kg/m^3$

$v$ is the velocity of the fluid flow $0.0075\ metre\ per\ second$

$D_h$ is the hydraulic diameter for the rectangular cross section

$\mu$ is the dynamic viscosity. As water is used as the fluid in this experiment, dynamic viscosity of water is $0.001002\ Pa.s$

$Reynolds\ number\ Re = \frac{1000\times0.0075\times0.1}{0.001002}$ = 748.5

Flow rate used: $3\ litres\ per\ minute$

Volumetric flow rate: $5 \times 10^{-5}\ cubic\ metre\ per\ second$

Cross sectional area of the test section: $0.01\ square\ metre$

Velocity of the flow: $\frac{Volumetric\ flow\ rate}{cross\ sectional\ area} = \frac{5\times10^{-5}}{0.01} = \ 0.005\ metre\ per\ second$

Since tank used is of rectangular cross section, Hydraulic diameter should be used, during the calculation of Reynolds number.

Hydraulic diameter $D_h = 0.1\ metre$

$$Reynolds\ number\ Re = \frac{\rho v D_h}{\mu}$$

$$Reynolds\ number\ Re = \frac{1000\times0.005\times0.1}{0.001002} = 499$$

With the Reynolds number known for both flow rates, the Strouhal number for each value can be calculated with the formula,

$$\text{Strouhal number } St = 0.198\left(1 - \frac{19.7}{Re}\right)$$

For Reynolds number with a value of 748.5,

$$\text{Strouhal number } St = 0.198\left(1 - \frac{19.7}{748.5}\right) = 0.1927$$

For the Reynolds number 499,

$$\text{Strouhal number } St = 0.198\left(1 - \frac{19.7}{499}\right) = 0.1901$$

The relation between Strouhal number and Reynolds number can be seen in the image below.

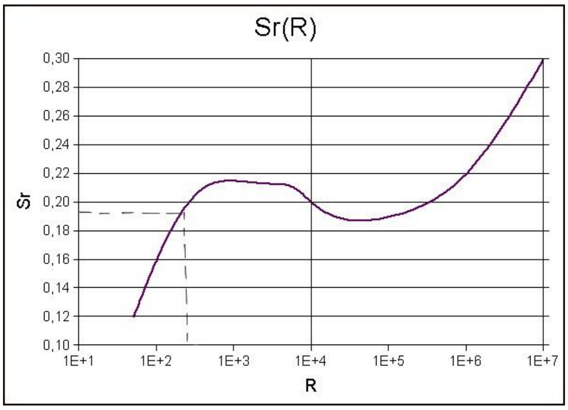


**Figure 43 Strouhal number relative to the Reynolds number**

The frequency at which the vortex shedding occurs is called vortex shedding frequency $f_w$. It can be related to Strouhal number $St$ with the hydraulic diameter or pipe diameter $d$, and the velocity of the fluid $V$ by the relation,

$$St = \frac{f_w d}{V}, \qquad and \quad f_w = \frac{StV}{d}$$

For velocity $0.0075$ $metre\ per\ second$, the Strouhal number is $0.1927$ and the hydraulic diameter is $0.1$ $metre$, therefore

$$f_w = \frac{StV}{d} = \frac{0.1927 \times 0.0075}{0.1} = 0.0145\ s^{-1}$$

For velocity $0.005$ $metre\ per\ second$, the Strouhal number is $0.1901$ and the hydraulic diameter is $0.1$ $metre$,

$$f_w = \frac{StV}{d} = \frac{0.1901 \times 0.005}{0.1} = 0.0095\ s^{-1}$$

# 6. RESULTS AND ANALYSIS

Results have been calculated for two Reynolds number for both the bluff bodies and the images are post processed using DaVis FlowMaster 10.0.4 software. The results have been analyzed for the velocity fields 10 $cms$ after the bluff body as the field of view.

## 6.1. RESULTS OF BLUFF BODY WITHOUT SLIT

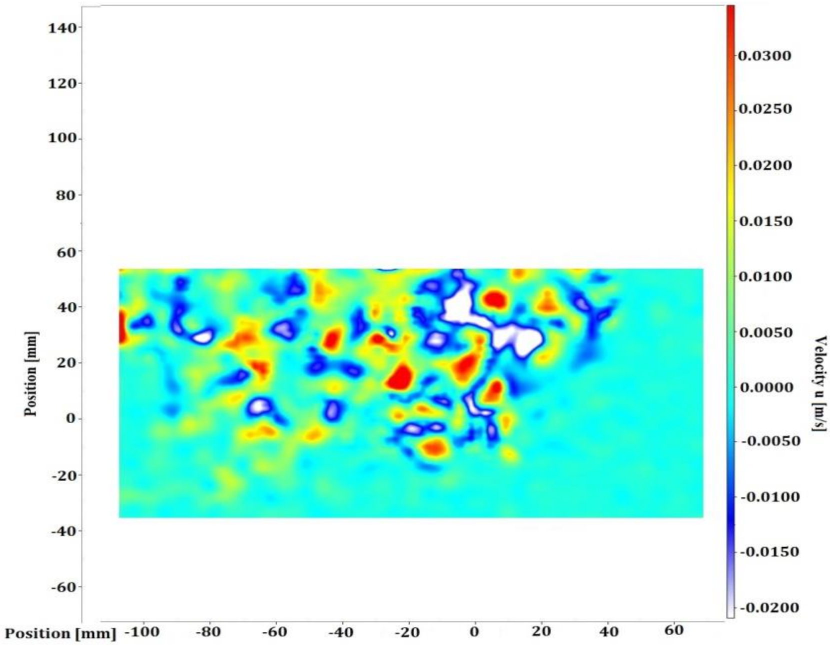


**Figure 44 U-component velocity versus position at Re=748.5**

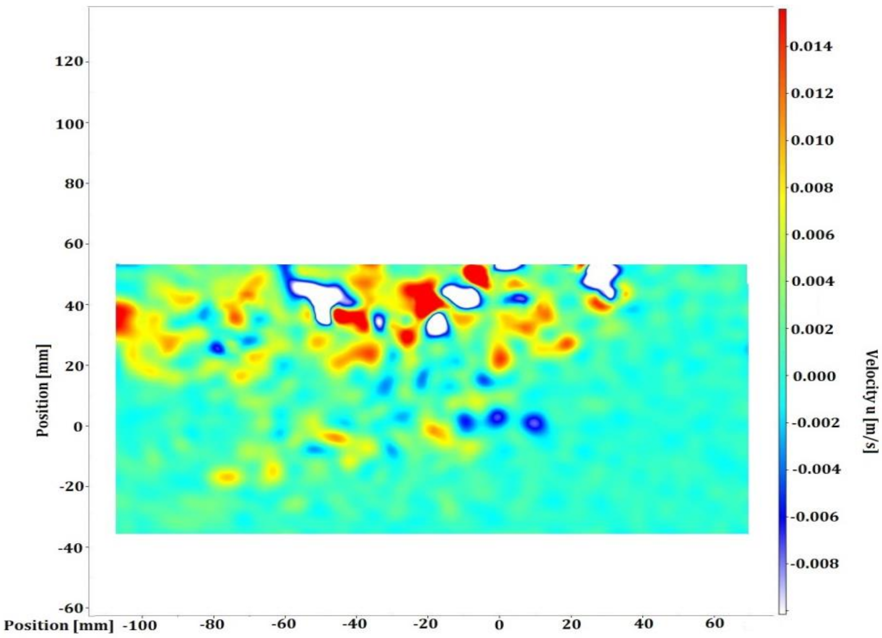


**Figure 45 U-component velocity versus position at Re=499**

Figure 44 and figure 45 shows the scalar field for the velocity component in u direction at Reynolds number 748.5 and 499 for the cylinder without slit. Wakes with alternating vortices can be noticed in both images behind the bluff body both upstream and downstream. It can be identified that the flow around bluff body at Reynolds number 499 shows a bit clearer length of the vortex street rather than the image at 748.5. It can be because of the velocity variation between both Reynolds number and the bubbles created due the external disturbances. It can be noted that the flow reattachment occurs at the immediate downstream of the locations where there is maximum pressure fluctuations. For Re=748.5, the velocity at the entrance is set to be 0.0075 m/s, and the maximum and minimum velocity are found to be 0.0300 and -0.0200 respectively. For Re=499, the initial velocity is 0.005 m/s, where the maximum and minimum velocities are identified to be 0.014 and -0.008.

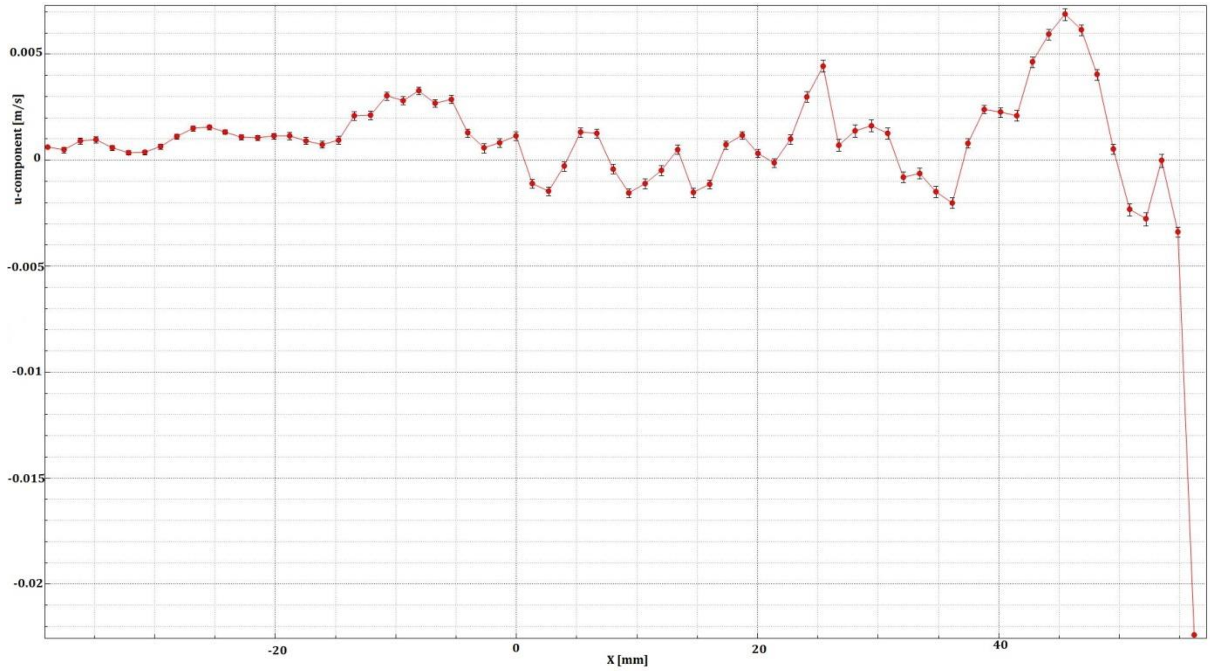


**Figure 46 Position versus u-component of velocity at Re=748.5**

Figure 46 and 47 shows the graphical representation of the values at Re=748.5. Figure 46 shows the values of u component of velocity with respect to the position along the field of view. The velocity remains constant and gets an alternating increase and decrease of the peaks because of the formation of vortices on both upstream and downstream. Figure 47 shows the value of vorticity along the field of view, from which the alternating high and low peaks can be interpreted as alternating vortices with high and low velocities.

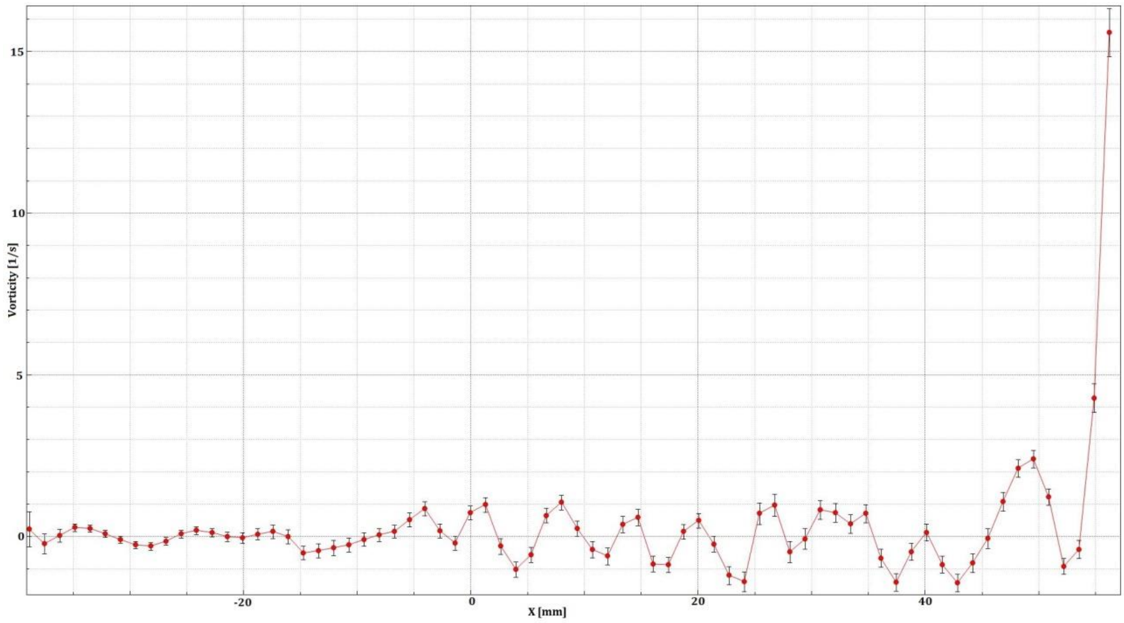


**Figure 47 Position versus values of vorticity at Re=748.5**

Figure 48 and Figure 49 shows the graphical representation of the velocity component in u direction and vorticity happened behind the bluff body at Re=499. Velocity graph shows that after the bluff body is being hit by the fluid, there is a reduction in the flow velocity because of the obstruction caused by bluff body. After the flow reattachment, the velocity tends to vary alternatively until it reaches the end. Alternating vortices with high and low peaks can be seen in Figure 49.

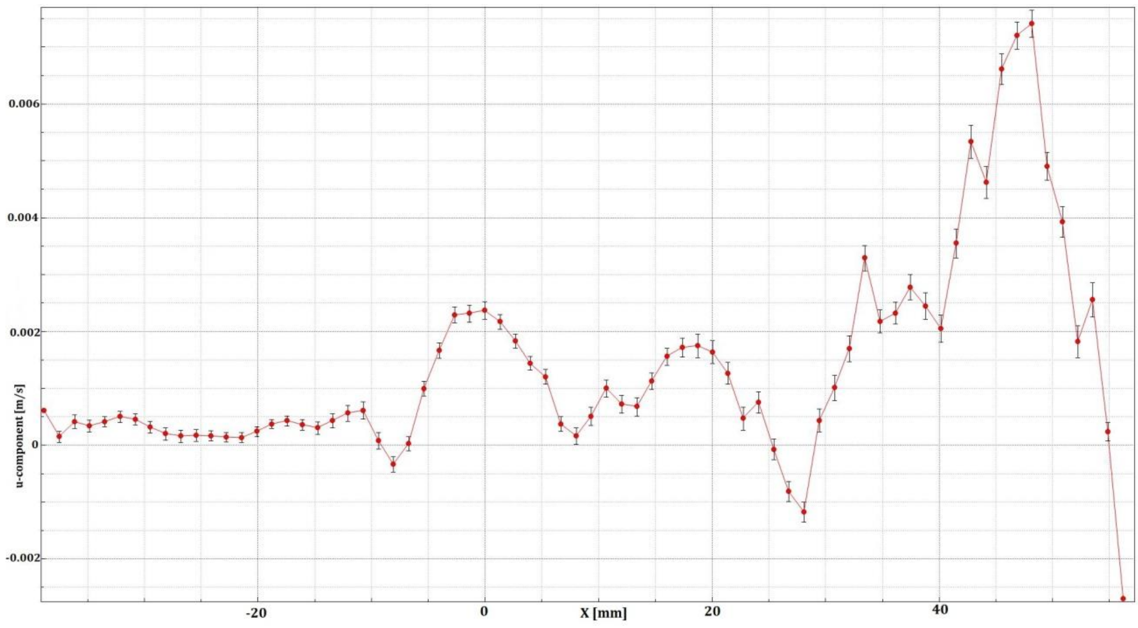


**Figure 48 Position versus u-component of velocity at Re=499**

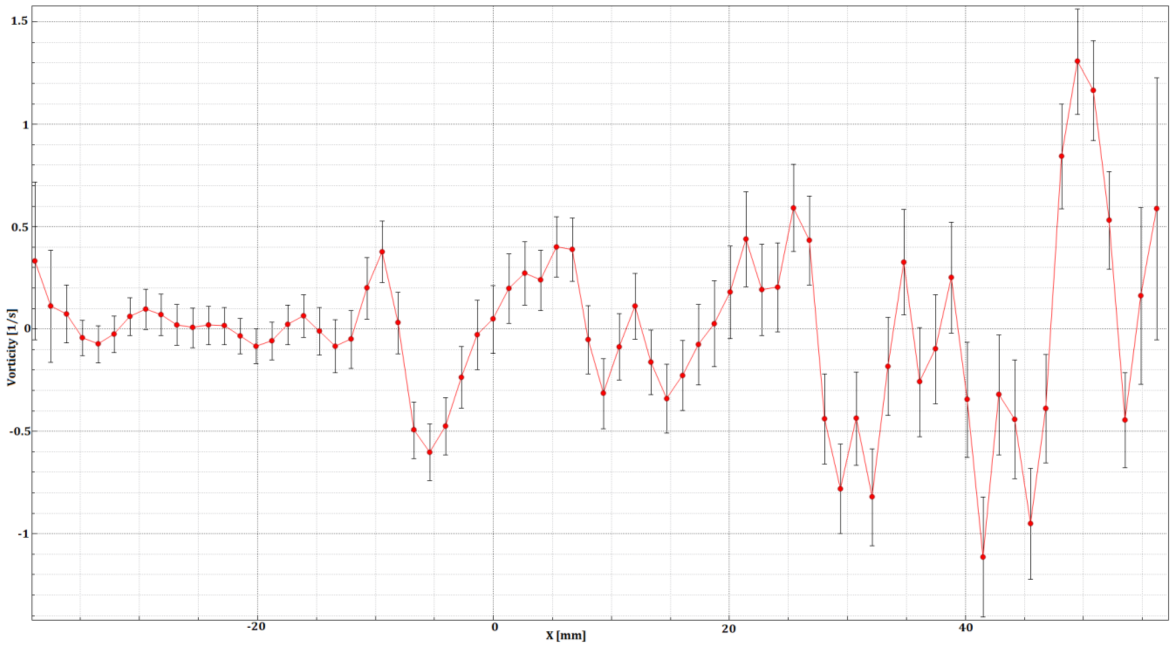


**Figure 49 Position versus values of vorticity at Re=499**

## 6.2. RESULTS OF BLUFF BODY WITH SLIT

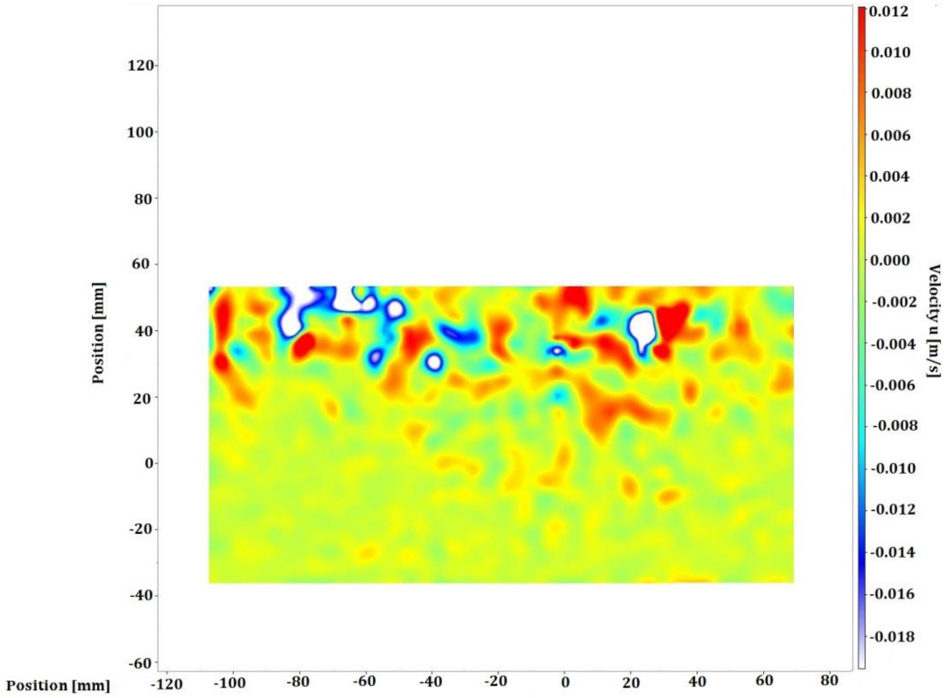


**Figure 50 U-component velocity versus position of bluff body at Re=748.5**

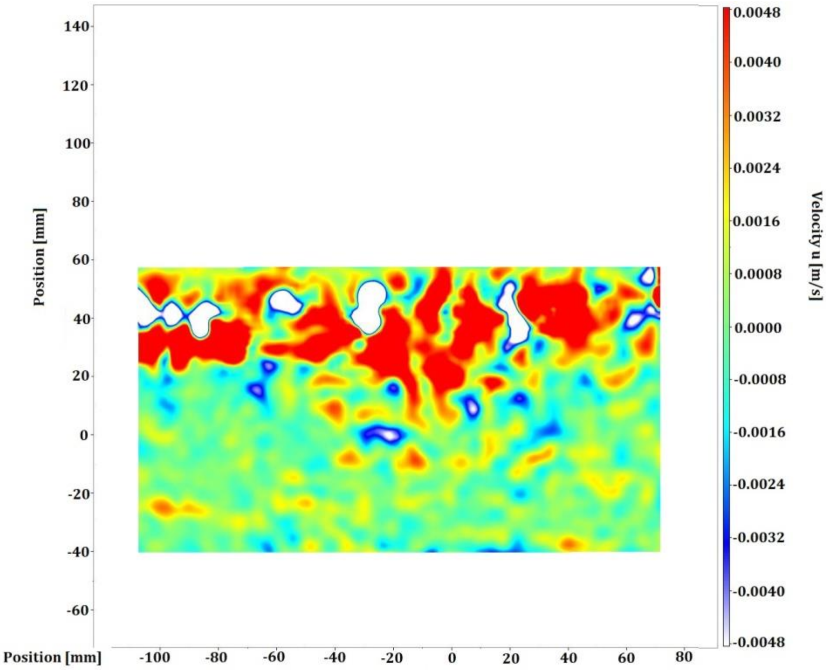


**Figure 51 U-component velocity versus position of bluff body at Re=499**

Figure 50 and 51 shows the velocity of the fluid in u direction flowing along the image plane after crossing the bluff body with slit at Re=748.5 and Re=499. It can be seen that the length of the vortex shedding cannot be identified clearly because of the turbulence caused by the water bubbles, geometry of the bluff body as the water passes through the slit and collapses the surrounding vortices caused.

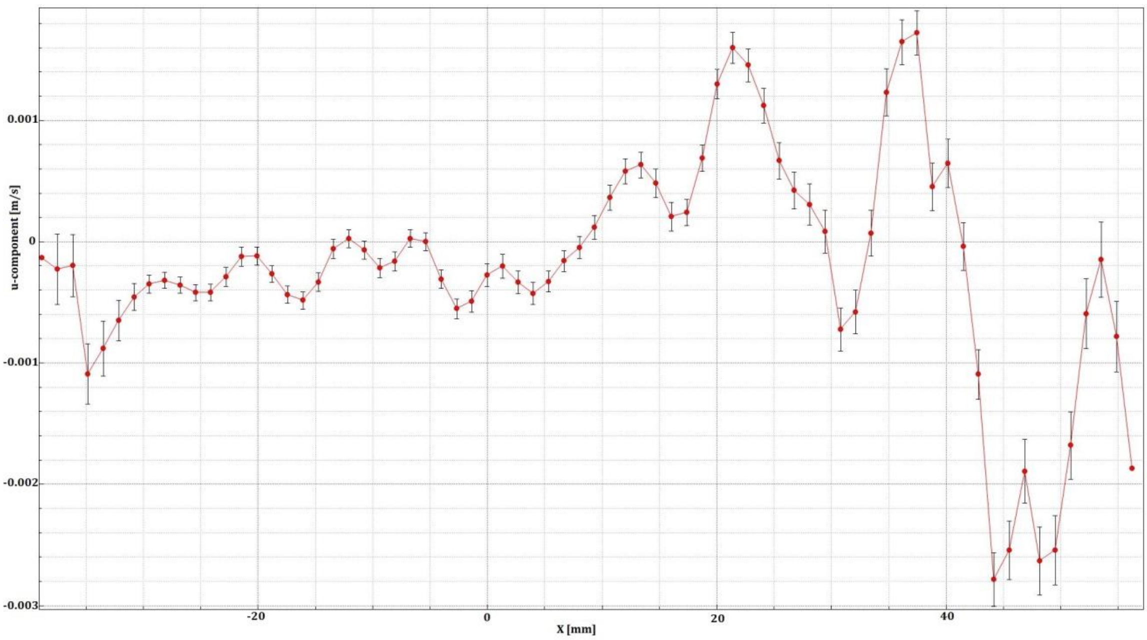


**Figure 52 Position versus u-component of velocity at Re=748.5**

Figure 52 and 53 shows the graphical representation of the values of u component velocity and vorticity versus position along the image plane at Re=748.5. The velocity and vorticities show higher value of fluctuation compared to the bluff body without slit. It can be noticed that the velocity reaches its maximum at relative position of 46 mm compared to the whole field of view.

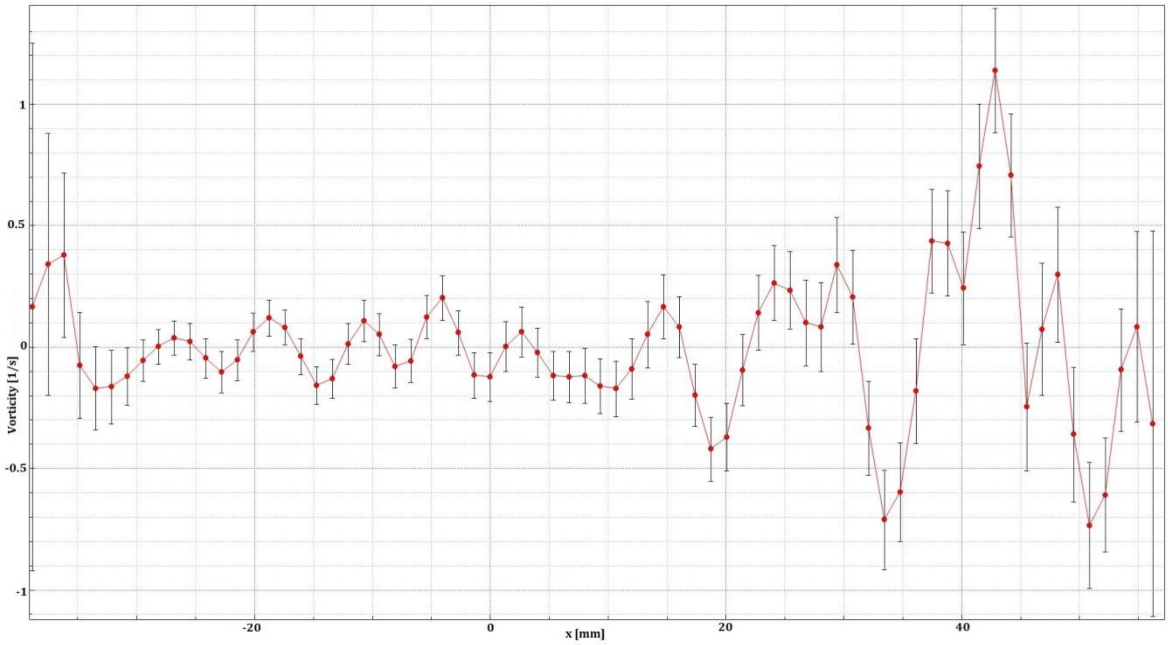


**Figure 53 Position versus values of vorticity at Re=748.5**

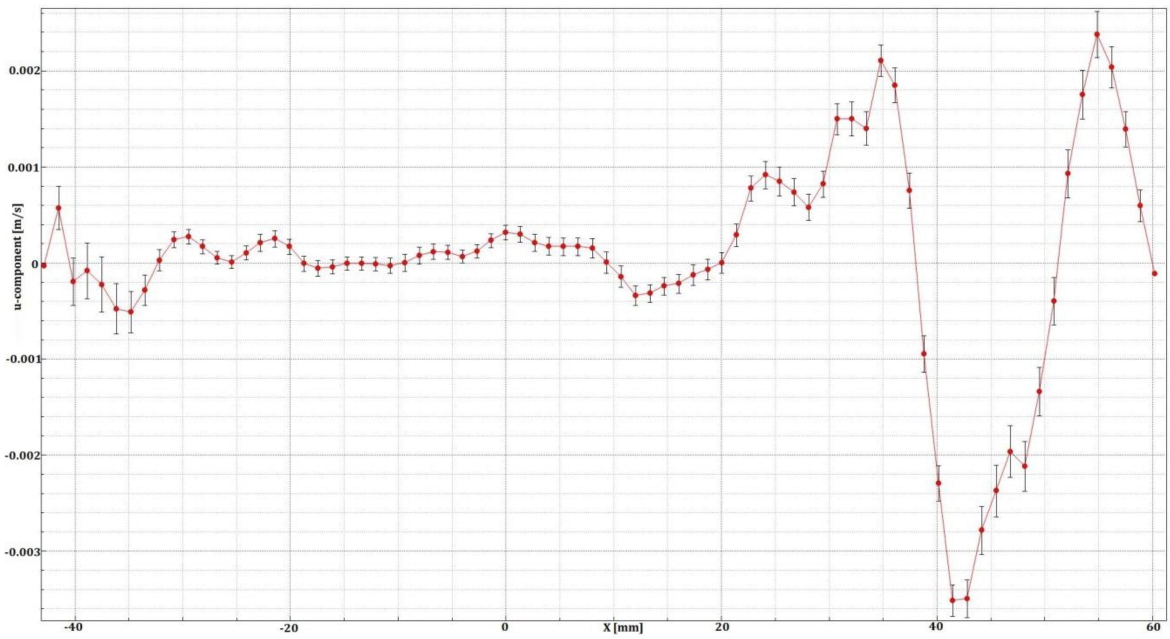


**Figure 54 Position versus u-component of velocity at Re=499**

Graphical representation of the system at Re=499, for velocity and vorticity are represented in images Figure 54 and Figure 55. Velocities and vorticities shows the highest variation compared to any other results combined. It can be because of the effect of reduced velocity with the geometry of the bluff body causing external disturbances. Velocity reaches a maximum of 0.0024 m/s at the end of the view field.

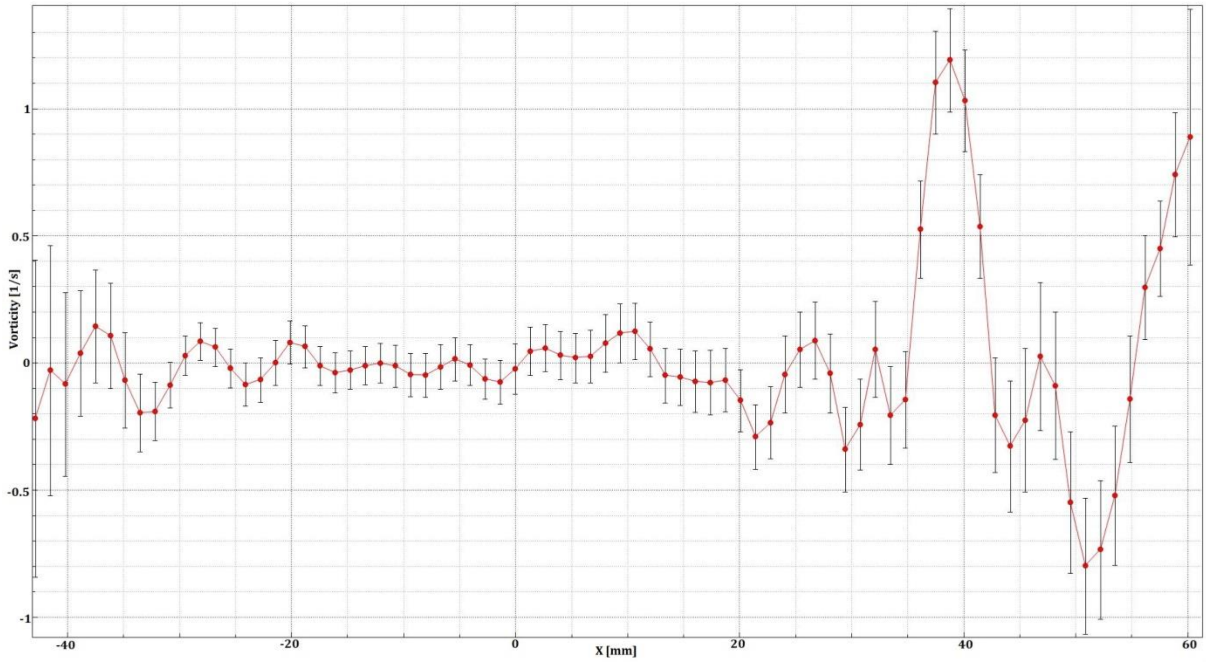


**Figure 55 Position versus values of vorticity at Re=499**

The experiment carried out with minimum synchronization implies the importance of synchronization to be done for future works. It can be noticed that at low range of liquid speed, the motion is not periodic until the critical velocity is reached, to get a flow oscillation in periodic manner increasing in amplitude, with increase in velocity.

# 7. CONCLUSION

The flow around the cylindrical bluff bodies with and without slit are investigated at two different Reynolds numbers 748.5 and 499 with water at room temperature as working fluid. The flows have been recorded and analyzed using Particle Image Velocimetry and Davis FlowMaster 10.0.4 software. Two dimensional images of the flow have been captured using planar PIV and analyzed for the properties. Detailed understanding of working and processing of planar PIV is obtained. The results obtained are related with the literature for examining the similarity between experimental and theoretical values. Results show that the flow around bluff body with complex geometry affects the properties of the flow at particular velocities. Understanding of Particle Image Velocimetry at a higher level is required to obtain the perfect results for the visualization. Alternating vortices are identified along the image plane both upstream and downstream, which shows the occurrence of vortex shedding. Minimum velocity alteration after the bluff body is identified for cylinder without slit compared to the cylinder with slit.

## 7.1. FUTURE WORK

This area of research can be improved by

- Examining the flow with varied Reynolds number
- Increasing the synchronization of the system
- Using different geometry of cylindrical bluff body
- Investigating and comparing a bluff body in multiple working fluids.

# REFERENCES


[1] P. L. VERMA and M. GOVARDHAN, “FLOW BEHIND BLUFF BODIES IN SIDE-BY-SIDE ARRANGEMENT,” *Journal of Engineering Science and Technology* , pp. 745-767, 2011.

[2] V. Oruç, “Strategies for the applications of flow control downstream of a bluff body,” *ELSEVIER,* 2017.

[3] R. D. Keane and R. J. Adrian, “Optimization of perticle image velocimeters,” pp. 1202-1215, 1990.

[4] J. Westerweel, D. Dabiri and M. Gharib, “The effect of a discrete window offset on the accuracy of cross-correlation analysis of digital PIV recordings,” *Springer-Verlag,* pp. 20-28, 1997.

[5] S. Chevula, A. Sanz-Andres and S. Franchini, “Aerodynamic external pressure loads on a semi-circular bluff body under wind gusts,” *ELSEVIER,* pp. 947-957, 2105.

[6] M. I. Yuce and D. A. Kareem, “A Numerical Analysis of Fluid Flow Around Circular and Square Cylinders,” *ResearchGate,* pp. 546-554, 2016.

[7] L. Huang, Y. Deng and B. Wang, “Bluff-body flow at different Reynolds number based on LAttice-Boltzmann method,” *JVE International,* pp. 48-55, 2016.

[8] S. V. Singh and N. K. M, “CFD Analysis of Different Bluff Bodies,” *Novelty Journals,* pp. 139-145, 2015.

[9] D. T. Prosser and M. J. Smith, “Characterization of flow around rectangular bluff bodies at angle of attack,” *ELSEVIER,* pp. 3204-3207, 2012.

[10] B. Levy and P. Brancher, “Experimental investigation of the wall dynamics of the A-pillar vortex flow,” *Elsevier,* pp. 540-545, 2015.

[11] S. Yagmur, S. Dogan, M. H. Aksoy, E. Canli and M. Ozgoren, “Experimental and Numerical Investigation of Flow Structures around Cylindrical Bluff Bodies,” *EPJ Web of Conferences,* pp. p.1-p.7, 2015.

[12] A. Alomar, D. Angland and X. Zhang, “Extension of roughness noise to bluff bodies using the boundary element method,” *ELSEVIER,* pp. 318-337, 2018.

[13] Z. J. Taylor, E. Palombi, R. Gurka and G. A. Kopp, “Features of turbulent flow around symmetric elongated bluff bodies,” *ELSEVIER,* pp. 250-265, 2011.

[14] K. H. Lo and K. Kontis, “Flow around an articulated lorry model,” *ELSEVIER,* pp. 58-

74, 2017.

[15] F. Scarano, “Iterative image deformation methods in PIV,” *Institute of Physics Publishing*, pp. R1-R19, 2002.

[16] B. Wieneke and A. Sciacchitano, “PIV UNcertainity Propagation,” *11th International Symposium on Particle Image Velocimetry*, pp. 1-19, 2015.

[17] Sojoodi, A. &. Saha and Suvash, “Shear Thinning and Shear Thickening Non-Newtonian Confined Fluid Flow over Rotating Cylinder,” *American Journal of Fluid Dynamics*, pp. 117-121, 2013.

[18] M. Bergstresser, “Reynolds number: Definition and Equation,” [Online]. Available: https://study.com/academy/lesson/reynolds-number-definition-equation.html. [Accessed 03 April 2019].

[19] Á. R and M. A, “Flow study over bluff bodies based on visualization technique,” *American Association for Science and Technology*, pp. 97-104, 2018.

[20] D. R. J. Adrian, “Introduction : Aerodynamics and friction losses,” [Online]. Available: www.efluids.com/efluids/pages/bicycle.htm.

[21] “drag on objects moving through fluids,” [Online]. Available: http://www.roymech.co.uk/Related/Fluids/Fluids_Drag.html.

[22] S. Yarusevych and P. Sullivan, “On vortex shedding from an airfoil in low Reynolds number flows,” *J. Fluid Mech.*, pp. 245-271, 2009.

[23] S. Kaneko and F. Inada, Flow Induced Vibrations, Elsevier Science, 2008.

[24] E. D. Gedikli, “Experimental investigation of low mode number cylinders subjected to vortex-induced vibrations,” *ResearchGate*, 2014.

[25] S. Bengt, “Vortex Shedding,” 16 March 2011. [Online]. Available: http://www.thermopedia.com/content/1247/. [Accessed April 2019].

[26] Jonathan Lucas Heseltine, “Flow around a circular cylinder with a free end,” Canada, 2003.

[27] C. M and D. J. R, “Circular cylinder wake configurations: a flow visualization study,” *Applied Mechanics Review*, pp. 255-305, 1991.

[28] D. Kröninger, K. Köhler, T. Kurz and W. Lauterborn, “Particle tracking velocimetry of the flow field around a collapsing cavitation bubble,” *SpringerLink*, pp. 395-408, 2010.

[29] “EduPIV - a turnkey PIV system for educational use,” [Online]. Available: https://www.dantecdynamics.com/edupiv-educational-piv-system.

[30] “Stereoscopic (2D3C) PIV,” [Online]. Available: https://www.piv.de/piv/stereoscopic_2d3c_piv.php.

[31] “Microfluidics,” [Online]. Available: https://www.dantecdynamics.com/microfluidics.

[32] M. A, “Tracer Particles and seeding for particle image velocimetry,” *Meas. Sci. Technol,* pp. 1406-1416, 1997.

[33] K. Ratkovská, “Particle Image Velocimetry,” Pilsen 2013.

[34] B. Morris, “Imaging Techniques for Flow and Motion Measurement,” 2011. [Online]. Available: https://slideplayer.com/slide/7279067/.

[35] W. B, “PIV Uncertainity Quantification and Beyond,” p. 211, 2017.

[36] B. R. J. M, “Cross-correlation PIV: theory, implementation and accuracy,” 2014.

[37] “PIV Analysis” [Online]. Available: https://www.dantecdynamics.com

[38] S. F, “Iterative image deformation methods in PIV,” 2001.